Journal Homepage: http://ijcpe.uobaghdad.edu.iq
Iraqi Journal of Chemical and Petroleum Engineering
Vol. 26 No. 3 (September 2025) 151 – 171
EISSN: 2618-0707, PISSN: 1997-4884

Geomechanical properties evaluation of Mauddud formation based on experimental measurements and well log data

Mohammed Almojahed F. Al-jumaili [a, *], Nagham J. Al-Ameri [a]

a Petroleum Engineering Department, College of Engineering, University of Baghdad, Baghdad, Iraq

Abstract

Mauddud formation is one of the most prominent formations in Northeastern Iraq due to its significant hydrocarbon reserves, making accurate geomechanical characterization essential for safe drilling operations and informed development planning. This study constructs a calibrated post-drill one dimensional mechanical earth model (1D-MEM) for selected wells, levering Techlog software to integrate rock mechanical data, image logs, multi-arm caliper measurements, conventional well logs, drilling reports, and core analyses. The methodology provides a detailed workflow for estimating geomechanical properties from log and image analysis to model calibration. Validation of the 1-D MEM performed through cross-comparison with direct measurements, ensuring the reliability of the predicted stress and strength profile. Laboratory and field data including pore pressure measurements using DST method, destructive and non-destructive mechanical tests, scanning electron microscopy (SEM), thin section test (TS), X-ray diffraction test (XRD), and energy-dispersive X-ray spectroscopy (EDS) have all been used for analyzation and calibration process. These datasets enhance the MEM parameters and support the derivation of empirical correlation specific to the Mauddud Formation. Derived correlations include compressional-shear slowness velocity, slowness velocity- bulk density, compression slowness-unconfined compressive strength (UCS), and the Young's modulus to UCS correlation. Results show that mineralogical composition particularly porosity and calcite content have a dominant influence on formation strength with high porosity, low calcite intervals resulting in the lowest UCS values.

Keywords: *Rock Mechanical Properties Evaluation; Experimental Rock Evaluation; UCS; X-Ray Diffraction; Scanning Electron Microscopy.*

Received on 16/01/2025, Received in Revised Form on 06/04/2025, Accepted on 10/04/2025, Published on 30/09/2025

https://doi.org/10.31699/IJCPE.2025.3.13

1- Introduction

Mauddud Formation is a significant carbonate reservoir located in the Arabian Plate region [1]. The formation is thick and exhibits a regional distribution across the Arabian plate [2, 3]. Oil is extracted from limestone formations in Badra oil field located in eastern Iraq, specifically from Mauddud Formation [4]. Mauddud Formation in Badra oil field consists of limestone with a thin dolomite coating, stylolitic dolomite, and detrital and chalky limestone. A substantial collection of fossils indicates an Albian age. It was initially believed that the formation extended into the Cenomanian, as demonstrated by the recurrent presence of specific Orbitolina concave group species [5]. The formation was deposited in a neritic environment, with occasional shoaling [5].

Badra field is situated in eastern part of Iraq, close to the borders between Iraq and Iran, as shown in Fig. 1A, [6]. The Badra field structure is an asymmetrical NW-SE anticline trending, with a more gradual NE flank and a sharply descending SW flank [5], Fig. 1B, show the distribution of two wells under study which are Well B and Well C. The formation is situated between the Mesopotamian Zone (Tigris subzone), and Foothill Zone (Himreen-Makhul subzone). The Mesopotamian zone represents the easternmost unit of the Stable Shelf. The region probably experienced an uplift during the Hercynian deformation, but it subsequently declined in the Late Permian period. The subsurface layer consists of concealed faulted structures interspersed with broad synclines, situated beneath the Quaternary cover. Fig. 1B, illustrates the presence of NE-SW trending fold structures. In the eastern region of the zone, these structures predominantly trend NW-SE, whereas in the southern region, they exhibit a N-S orientation [7].The Mesopotamian Zone comprises three subzones: the Tigris, Euphrates, and Zubair subzones.

The Tigris Subzone is the biggest and most movable unit in the Mesopotamian Zone. In addition to minor anticlines and large synclines that trend NW-SE, there are lengthy normal faults. The zone is characterized by an EW transversal trend as well as two sets of buried anticlines that trend NW-SE and are connected to longitudinal faults [8].

This segment of the Unstable Shelf is designated as the Foothill Zone. It comprises exceptionally thick Miocene-Pliocene molasses sediments, measuring 3 kilometers in thickness, and the deepest Precambrian basement in Iraq, reaching 13 kilometers. The zone is divided into two longitudinal components: Makhul-Hemrin Subzone in the southwest and Butmah-Chemhemal Subzone in the

---

*Corresponding Author: Email: muhammed.farooq2208M@coeng.uobaghdad.edu.iq

northeast. The structurally deepest region of the Foothill Zone is the Makhul-Hemrin Subzone, characterized by prominent NW-SE or E-W trending anticlines associated with decollement thrust faults. These anticlines extend over 100 kilometers [7]. The Badra field structure is an asymmetrical NW-SE trending anticline, featuring a more gradual NE flank and a sharply descending SW flank [5].

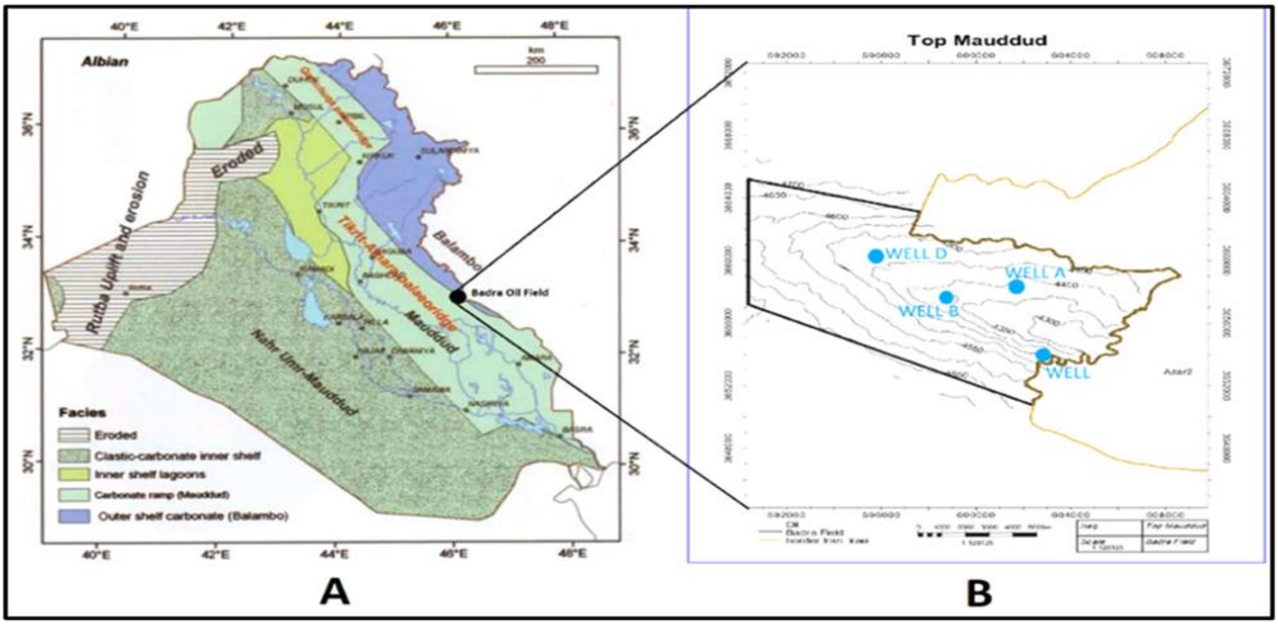

Fig. 1. A) Location of the field under study on geological Iraqi map [7]. B) Well's location in the studied area

At its base, Mauddud Formation contacts Nahr Umr, Lower Balambo, and Lower Sarmod formations in a conformable and gradational manner, as shown in Fig. 2. In North Central, Northern, and Northeastern Iraq, there is an unconformity represented by the top contact, which is nonsequential and has a break [7].

Mechanical characteristics of rocks are assessed using two primary methodologies: destructive and non-destructive. Destructive techniques are used to derive stress-strain relationships and static mechanical characteristics from core samples, while non-destructive techniques rely on transmitting ultrasonic waves through core samples to ascertain dynamic mechanical characteristics, [9]. The crucial step after the experimental assessment is to identify a transformation function that correlates static and dynamic elastic parameters, [10]. Many authors try to find specific correlations for the various formations. Static and dynamic parameters were obtained experimentally under varying pressure and temperature conditions, and a correlation function was identified and analyzed, [11]. Well logs are essential tools used to correlating dynamic and static mechanical qualities tested in the lab with the parameters needed to calibrate the one-dimensional mechanical earth model, [12]. Understanding rock mechanical properties is essential for analyzing and modeling earth stress, borehole stability during drilling, sand production, and hydraulic fracturing. Static procedures involve laboratory testing with specialized equipment using core samples to assess their mechanical characteristics. Dynamic approaches involve computing compressional slowness (Dtc) and shear slowness (Dts), which can be obtained from logs [13]. Both laboratory tests and well log methods are essential for measuring rock mechanical characteristics [14]. Emphasis was placed on evaluating the mechanical properties of the Zubair Formation to enhance future development. The study included multi-stage triaxial testing. The results show a strong correlation between the predicted mechanical properties derived from logs and those observed in the laboratory, [15]. In fact, the triaxial compressive test represents a highly adaptable method for evaluating the strength of rock sample and provide facilitating the determination of its cohesion (c) and angle of internal friction (φ). The tool is capable of measuring both total and effective stress parameters and is applicable to all rock types. Drainage conditions are subject to control, and measurements of pore water pressure and volume changes can be conducted in accuracy [8, 9].

Mineral types and percentage play a crucial role in influencing the geomechanical properties of reservoirs. Measurement or determination of the mineralogical content of the samples is required. Different types of data, such as those obtained from a scanning electron microscope (SEM), thin section (TS) pictures, X-ray diffraction (XRD), and nuclear magnetic resonance (NMR), were utilized by the authors in order to correcting geomechanical properties [18]. They concluded that the geometry of the pores is a significant factor in determining how the permeability of consolidated and unconsolidated rock samples changes in response to stress. For the purpose of concentrating on the significance of the microstructural properties of rock with regard to stress-permeability, a comparable body of studies was conducted. Based on laboratory research (NMR and XRD), has provided an explanation for how reservoir stressors create microscopic strain at the pore size and how this strain affects the movement of fluids [19].

The X-Ray Diffraction (XRD) test conducted by many authors to quantify mineralogical percentages, thereby supporting the analytical results [20]. In the field of geomechanical properties research, scanning electron microscopy (SEM) is a direct approximation that can be used to analyze the specifics of porous networks and the microstructural characteristics. This is accomplished by observing full-diameter core sections in order to assess the presence of fractures and vugs. In addition to the prediction of the rock's mechanical properties and hydraulic behavior, the detection of cracks distribution and geometry in images is of great importance in the interpretation of anisotropy data. This is because cracks are a highly significant part of the rock's structure [16].

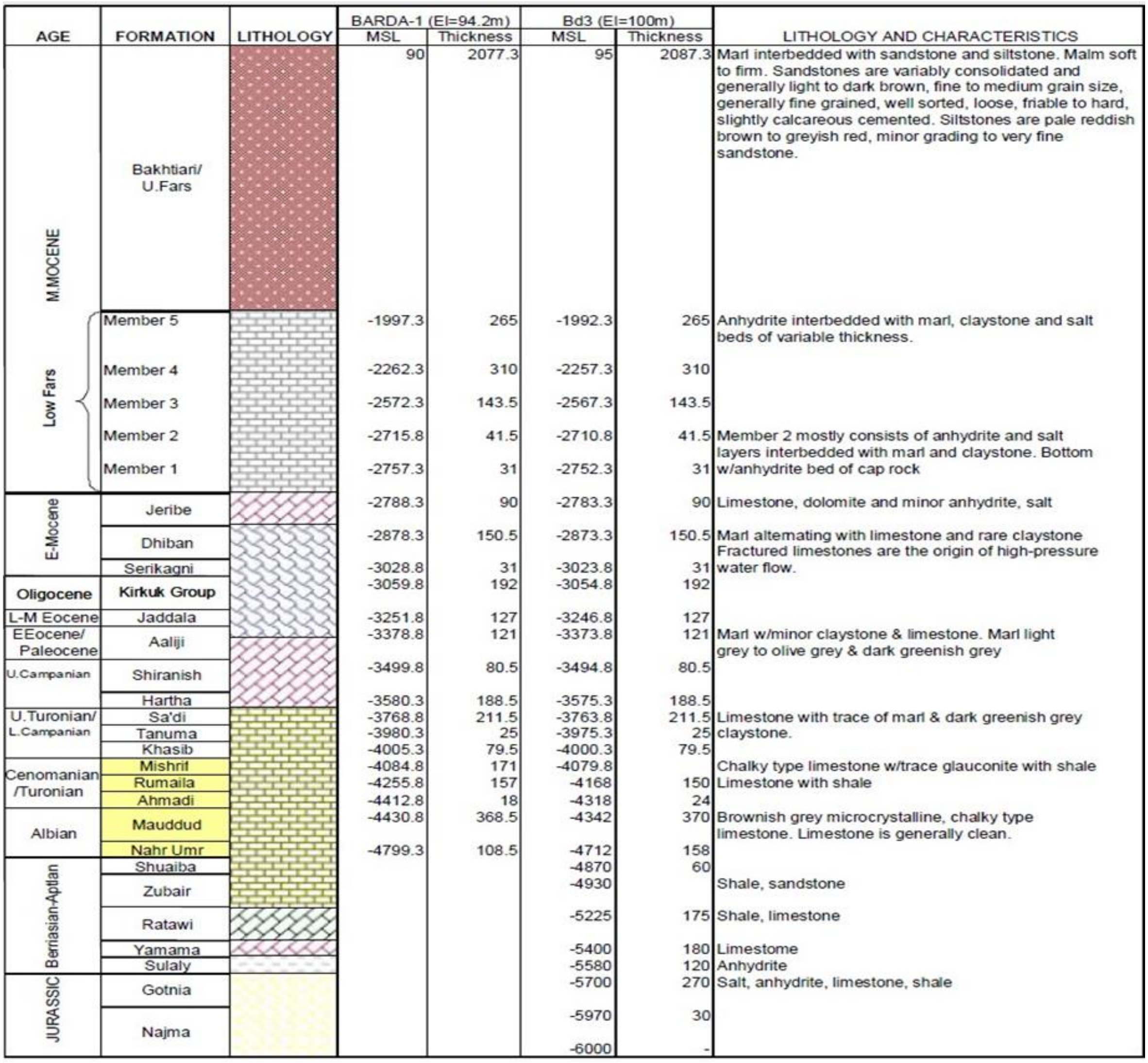

AGE	FORMATION	LITHOLOGY	BARDA-1 (El=94.2m) MSL	BARDA-1 (El=94.2m) Thickness	Bd3 (El=100m) MSL	Bd3 (El=100m) Thickness	LITHOLOGY AND CHARACTERISTICS
M.MOCENE	Bakhtiari/ U.Fars		90	2077.3	95	2087.3	Marl interbedded with sandstone and siltstone. Malm soft to firm. Sandstones are variably consolidated and generally light to dark brown, fine to medium grain size, generally fine grained, well sorted, loose, friable to hard, slightly calcareous cemented. Siltstones are pale reddish brown to greyish red, minor grading to very fine sandstone.
Low Fars	Member 5		-1997.3	265	-1992.3	265	Anhydrite interbedded with marl, claystone and salt beds of variable thickness.
	Member 4		-2262.3	310	-2257.3	310	
	Member 3		-2572.3	143.5	-2567.3	143.5	
	Member 2		-2715.8	41.5	-2710.8	41.5	Member 2 mostly consists of anhydrite and salt layers interbedded with marl and claystone. Bottom w/anhydrite bed of cap rock
	Member 1		-2757.3	31	-2752.3	31	
E-Mocene	Jeribe		-2788.3	90	-2783.3	90	Limestone, dolomite and minor anhydrite, salt
	Dhiban		-2878.3	150.5	-2873.3	150.5	Marl alternating with limestone and rare claystone Fractured limestones are the origin of high-pressure water flow.
	Serikagni		-3028.8	31	-3023.8	31	
Oligocene	**Kirkuk Group**		-3059.8	192	-3054.8	192	
L-M Eocene	Jaddala		-3251.8	127	-3246.8	127	
EEocene/ Paleocene	Aaliji		-3378.8	121	-3373.8	121	Marl w/minor claystone & limestone. Marl light grey to olive grey & dark greenish grey
U.Campanian	Shiranish		-3499.8	80.5	-3494.8	80.5	
	Hartha		-3580.3	188.5	-3575.3	188.5	
U.Turonian/ L.Campanian	Sa'di		-3768.8	211.5	-3763.8	211.5	Limestone with trace of marl & dark greenish grey claystone.
	Tanuma		-3980.3	25	-3975.3	25	
	Khasib		-4005.3	79.5	-4000.3	79.5	
Cenomanian /Turonian	Mishrif		-4084.8	171	-4079.8		Chalky type limestone w/trace glauconite with shale
	Rumaila		-4255.8	157	-4168	150	Limestone with shale
	Ahmadi		-4412.8	18	-4318	24	
Albian	Mauddud		-4430.8	368.5	-4342	370	Brownish grey microcrystalline, chalky type limestone. Limestone is generally clean.
	Nahr Umr		-4799.3	108.5	-4712	158	
Berriasian-Aptian	Shuaiba				-4870	60	
	Zubair				-4930		Shale, sandstone
	Ratawi				-5225	175	Shale, limestone
	Yamama				-5400	180	Limestome
	Sulaly				-5580	120	Anhydrite
JURASSIC	Gotnia				-5700	270	Salt, anhydrite, limestone, shale
	Najma				-5970	30	
					-6000	-	

Fig. 2. Stratigraphy column of the area of study [7]

Many researchers used a mixed approach, combining nanoindentation with scanning electron microscopy (SEM) and energy dispersive spectroscopy (EDX). With the application of EDS mapping over the grid indentation, It was discovered a connection between the scanned region's elemental heterogeneity and the variation in indentation findings, [21]. It was indented Marcellus shales with a variety of lithofacies using grids. The mineralogy of each indent was then determined by observing it with SEM and SEM-EDS. They looked at how different lithofacies affect the characteristics of the different phases [22]. Scanning electron microscopy (SEM) and energy-dispersive spectroscopy (EDS) analysis have yielded a novel method for determining the relationship between rock indentation and mineralogical properties; this method is known as an indentation test. A Pearson correlation analysis was used to investigate the connections between mechanical behaviors, elastic, plastic, and maximum indentation depths, indentation Young's modulus, hardness, and other mineralogical data [23].

This study has reported a number of different methods that were used to analyze and calibrate the software results. These methods include measurements of pore pressure using the DST method, measurements of destructive and non-destructive mechanical properties, a scanning electron microscopy (SEM) image, a thin section (TS) image test, an X-ray diffraction test, and an Energy-Dispersive X-ray spectroscopy (EDS) test. A correlation that was generated through experimentation was also produced in this study for the purpose of providing an accurate assessment of the geomechanical parameters of the formation that were of interest. There are several correlations that have been derived, including a correlation between compressional and shear slowness velocity, correlations between slowness velocity and bulk density, a correlation between compression slowness and unconfined compressive strength (UCS), particularly for Mauddud formation, and the relationship between Young's modulus and UCS. Based on the results of the tests, it is evident that the mineral type and proportion are highly influential factors on the strength of the formation. Low UCS intervals are the consequence of the majority of samples that have wide pore vogues and a low proportion of calcite minerals.

Geomechanical analysis is infrequently utilised in the Iraqi oil fields, except for a few studies conducted in the Badra oil field. Consequently, this study is regarded as one of the most reliable sources for further research. The experimentally derived correlation in this study can provide specialist equations to accurately construct a mechanical model.

2- Materials and methods

2.1. Mechanical earth model

Mechanical Earth Model (MEM) the stress state and rock mechanical properties for a specific stratigraphic section within the reservoir. The methodology for constructing the 1-D MEM model has been extensively documented by various authors [10, 25]. The calculation procedure workflow is illustrated in Fig. 3, comprises the procedures for constructing and calibrating the model to estimate pore pressure, fracture pressure, mechanical rock properties and minimum and maximum horizontal stresses.

The initial step involved gathering the data needed for the Mauddud formation to construct the model. The fundamental data necessary for constructing the model were well logs (density, compression wave velocities, porosity, shear wave velocities, gamma ray, and calliper) and core measurement data, such as measured mechanical properties from the triaxial core test. The last stage involves evaluating the quality of the data gathered by the standards set. Subsequently, the model was developed using data from the open-hole wireline logs.

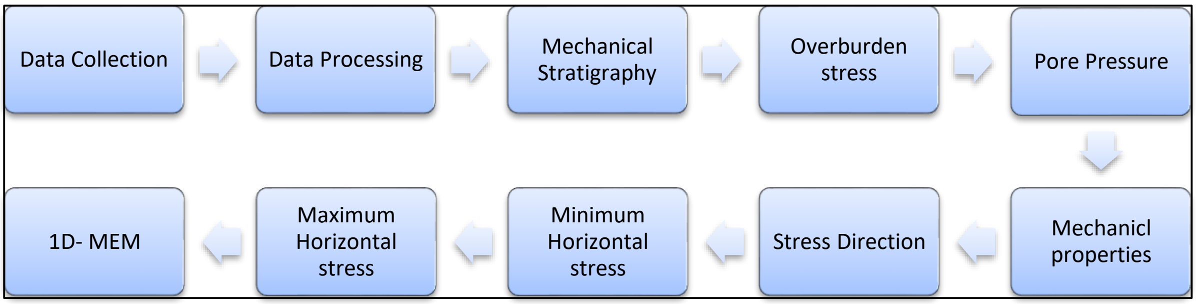

Fig. 3. Workflow of geomechanical modeling

2.1.1. Vertical stress

Vertical stress, also known as overburden stress, is brought on by the weight of the formations above. The density log can determine the vertical stress based on the depth of interest as shown in Eq. 1. Multiple techniques exist for estimating the bulk density. In this research, the extrapolated density method can produce satisfactory results for vertical stress, Eq. 2 [25]. Ao and α are the fitting parameters, and ρ midline is the seafloor or ground-level density [26].

$$\sigma v = \rho w * g * Zw + g\,\rho b * \int_{zw}^{z} Zdz \qquad (1)$$

$$\rho\, extrapolation = \rho\, mudline + Ao \times (TVD - Air\ gap - Water\ Depth)^{\alpha} \qquad (2)$$

Where: σv is the vertical stress, Zw is the water depth (for onshore drilling, Zw = 0); ρ_w is the density of seawater, and ρb is the formation bulk density as a function of depth.

2.1.2. Pore pressure and fracture pressure

The total pressure at a specific point in a formation is the sum of effective pressure and pore pressure [11, 12]. The effective stress reduces as pore pressure increases, raising the probability of failure [28]. Consequently, effective stress is defined as the difference between the externally applied stress and the internal pore pressure, as established by Terzaghi, or as the net stress exerted on the rock skeleton, Eq. 3:

$$\sigma` = \sigma - Pp \qquad (3)$$

Where: σ` = effective stress, σ = total stress, P_p = pore pressure. The poroelastic (α) or biot coefficient is the difference between bulk and pore volumes and explains the inter-grain connections between grains.

Next, the effective stress equation is written as follows [29], Eq. 4:

$$\sigma` = \sigma - \alpha\, Pp \tag{4}$$

The poroelastic constant ranges from zero to one. In low-stiff rocks, the Biot coefficient (α) equals zero. Conversely, for stiff rocks, α equals one. Therefore, the pore fluid plays a significant role in minimizing effective stress. As noted by [30], Eaton's technique [31] is the most common approach for predicting pore pressure in the oil and gas industry. This technique establishes an empirical relationship for calculating pore pressure based on compressional transit time data, as originally presented by Terzaghi [32]. This approach assumes that the overburden pressure is supported by both pore pressure and vertical effective stress, identifying the disequilibrium of compaction as the primary cause of overpressure. In this study, the non-shale zone Pp was calculated using sonic log as illustrated below in Eq. 5. [33]:

$$Pp = \sigma v - (\sigma v - Ppn) * a * \left(\frac{\Delta tn}{\Delta t}\right)^{n} \tag{5}$$

Where Δt represents the compressional transit time or slowness derived from the sonic log, while Δtn denotes the compressional transit time or slowness in shales under normal pressure conditions. The fitting factors "a" and "n" are called the Eaton exponent and Eaton factor, respectively. The initial parameters are n=3 and a=1. Ppn represents hydrostatic pore pressure.

Fracture pressure is the value at which a rock formation fractures, potentially resulting in the penetration of drilling fluids into adjacent formations. Eaton determined the fracture pressure by employing the formation's Poisson's ratio and the Hubbert and Willis concept of the minimum injection pressure, as illustrated in Eq. 6. [34, 28]:

$$Pf = \frac{v}{1-v}(\sigma v - \alpha\, Pp) + \alpha\, Pp \tag{6}$$

Pf = the fracture pressure (psi), v = Poisson's ratio.

2.2. Rock mechanical properties

The assessment of mechanical rock properties is crucial in geomechanical analysis. The fundamental mechanical properties of rock involve elastic properties: [Poisson's ratio (V: measuring the rock expands about a shortening in the axial direction), and Young's modulus (E: the resistance of a rock specimen to uniaxial stress), shear modulus (G: which defines the deformation of rock in response to shear stress), and the Bulk modulus (K: which measures the resistance to volumetric compression)], and strength properties: [internal friction angle (φ: an estimate of rock failure), unconfined compressive strength (UCS: The maximum compressive stress that a rock can handle in a triaxial test before it fractures), and cohesion (the amount of adhesion between linked molecules), tensile strength (TS: the most stress that a substance can take while being pulled before it breaks)].

Continuous profiles of these properties can strongly reflect the natural variability of strength and formation competency across all layers of the studied area. This work assessed mechanical rock parameters utilizing derived equations compatible with five log types: bulk density (ρb), compression slowness (DTc), shear slowness (DTs), gamma ray, and porosity [35]. One of the available efficient correlations must be used to transform the dynamic properties generated from logs into static properties .Because of factors such as cementation, pore pressure, amplitude, and rate of stress-strain [36], as well as the relatively loose constraints of the logging device [37], dynamic properties are usually greater than static ones.

Elastic properties including Poisson's ratio and Young's modulus are computed using shear, compressional, and bulk density logs [38]. As illustrated in Eq. 7, Eq. 8, Eq. 9 and Eq. 10:

$$G_{\ dyn=}13474.45\ \frac{\rho b}{DT^2{}_S} \tag{7}$$

$$K_{\ dyn=}13474.45\ \left(\frac{\rho b}{DT^2{}_C}\right) - \frac{4}{3}G_{dyn} \tag{8}$$

$$E_{dyn} = \frac{9G_{dyn}*K_{dyn}}{G_{dyn}+3K_{dyn}} \tag{9}$$

$$V_{dyn} = \frac{3K_{dyn}-2G_{dyn}}{6K_{dyn}+2G_{dyn}} \tag{10}$$

Where: Kdyn: dynamic bulk modulus (Mpsi), Gdyn: dynamic shear modulus (Mpsi), Vdyn: dynamic Poisson's ratio, and Edyn: dynamic Young's modulus (Mpsi).

After the determination of dynamic mechanical properties from the equation above, static properties must be determined. The most popular properties are static Young's modulus and static passion ratio. Some of the various correlations that can be used to transform dynamic Young's moduli into static ones include the Morales, Modified Morales, Plumb Bradford, and John Fuller correlations [14]. In this study John Fuller's correlation is used to estimate the static young modulus; since it is the most reliable correlation, it matches estimated and measured data well. In contrast, the static Poisson ratio was calculated by multiplying the dynamic Poisson ratio with a coefficient to convert it to the static Poisson ratio [39]. The static Young’s moduli and Poisson’s ratio computations were calibrated using Triaxial test points (TXT) obtained from a core work conducted in the Badra oil field, core intervals (4590-4595 m) and (4625 m) [40].

2.2.1. Unconfined compressive strength

Unconfined compressive strength UCS substantially impacts wellbore stability, as it plays a critical role when determining the failure criterion [38]. Consequently, the estimation of compressive strength must be accurate, as it serves as the final basis for subsequent calculations [39]. In order to achieve improved outcomes and minimize problems, various models have been used in the current study. Table 1 summarize six empirical equations that correlate the strength of limestone and dolomite with quantifiable petrophysical characteristics. Limestone and dolomite are examined collectively as a single carbonate rock group due to inadequate data to distinguish the correlation between strength and mechanical qualities of the various rock types. Unluckily, this leads to an exceptionally broad range of strength in limestone and/or dolomite for any specified parameter. At low porosity, high velocity, strength fluctuates by almost a factor of four, irrespective of whether velocity, or porosity were used for determining strength. Consequently, empirical equations that correlate the strength of carbonate rocks with geophysical variables poorly address the relationships involving velocity, or porosity data, underscoring the necessity of calibrating strength in every individual case.

Table 1. Summary of published empirical correlations for calculating the UCS

Eq. No.	UCS(MPa)	General comments	Reference
1	$\exp(-6.95\ \Phi)^{143.8}$	Representing low to moderate porosity ($0.05<\phi<0.2$) and high UCS)30 >UCS<150 MPa(	[41]
2	$276*(1-3*\Phi)^2$	Korobcheyev deposit, Russia	[41]
3	$135.9\exp(-4.8\ \Phi)$	Representing low to moderate porosity ($0<\phi<0.2$) and high UCS)10 >UCS<300 MPa(	[41]
4	$194.4-0.6072*Dtc-646.1\ \Phi\ -0.016444*Dtc^2 + 8.792(\Phi*Dtc)$	Limestone with 40< UCS<160 MPa	[42]
5	$(7682/Dtc)^{1.82}/145$	General	[42]
6	$10^{(2.44+109.14/Dtc)}/145$	General	[42]

Where Φ is porosity (unitless fraction) and DTc is the compression slowness (us/ft).

2.2.2. Friction angle and tensile strength

Friction angle is determined by correlating gamma ray measurements to the friction angle using a linear connection [45], as shown in Fig. 4. A cutoff is implemented for the friction angle. Using the default parameters, Gamma ray 120 gAPI corresponds to FANG 20 degrees, while Gamma ray 40 gAPI corresponds to FANG 35 degrees. If the calculated FANG is below 15 degrees, it is adjusted to 15 degrees. If it exceeds 40 degrees, it is constrained to 40 degrees. The default parameters can be modified. The model offers simple correlation for calculating tensile strength using UCS strength [23, 24]. As shown Eq. 11 below:

$$TS = K * USC \tag{11}$$

Where TS is tensile strength (psi), K is the zone-based factor and facies, the use of 0.95 gives good agreement.

2.3. Horizontal stress (minimum and maximum)

The next step in constructing the mechanical earth model involves calculating the principal horizontal stresses, specifically the minimum and maximum horizontal stresses, and determining their orientations while acknowledging that vertical stress is also a principal stress. The minimum and maximum horizontal stress magnitudes are calculated using the static Poisson's ratio, the static Young's Modulus derived from the John-Fuller correlation, overburden pressure (vertical stress), and pore pressure as inputs. The Techlog software (2015) introduced the Poro-Elastic strains model, recognized as the predominant method for calculating in-situ horizontal stresses, as in Eq. 12 and Eq. 13 below:

$$\sigma H = \frac{v}{1-v}\sigma v - \frac{v}{1-v}\alpha\ Pp + \alpha\ Pp + \frac{E}{1-v^2}\varepsilon H + \frac{vE}{1-v^2}\varepsilon h \tag{12}$$

$$\sigma h = \frac{v}{1-v}\sigma v - \frac{v}{1-v}\alpha\ Pp + \alpha\ Pp + \frac{E}{1-v^2}\varepsilon h + \frac{vE}{1-v^2}\varepsilon H \tag{13}$$

In these equations, σv represents overburden stress (psi), Pp represents pore pressure (psi), σH and σh represent maximum and minimum horizontal stresses (psi), α=1 represents Biot's coefficient, εH and εh are the strain in the direction of σH and σh, respectively, as expressed in Eq. 14 and Eq. 15 below:

$$\varepsilon h = \frac{Pp*\sigma v}{E}\left(1 - \frac{v^2}{1-v}\right) \tag{14}$$

$$\varepsilon H = \frac{Pp*\sigma v}{E}\left(\frac{v^2}{1-v} - 1\right) \tag{15}$$

The orientations of horizontal in-situ stress fields are also crucial for interpreting the stress field, which is necessary for borehole failure analysis [48]. A caliper log is used for determining the orientation of the wellbore breakout, parallel with the direction of minimum horizontal stress (σh) and perpendicular to the maximum horizontal stress (σH) [49].

Fig. 5, illustrates the regional director of σH, around 40-50 degrees, influenced by various physical data (e.g., wellbore breakouts, earthquakes, etc.).

3- Experimental evaluation of mauddud formation

The assessment of the mechanical properties of samples can be performed utilizing understanding the mineralogical analysis conducted using X-ray diffraction (XRD), along with rock texture analysis obtained through Scanning Electron Microscopy (SEM) and Thin Section (TS) testing, employing Energy-Dispersive X-ray spectroscopy (EDS) for chemical characterization and elemental analysis of materials. A prior understanding of these factors is crucial in oil industry applications. Two samples extracted from Mauddud formation have been utilized for experimental measurement, as seen in Fig. 6.

These samples are extracted from two wells. The samples utilized in this test are cutting samples with an inconsistent form.

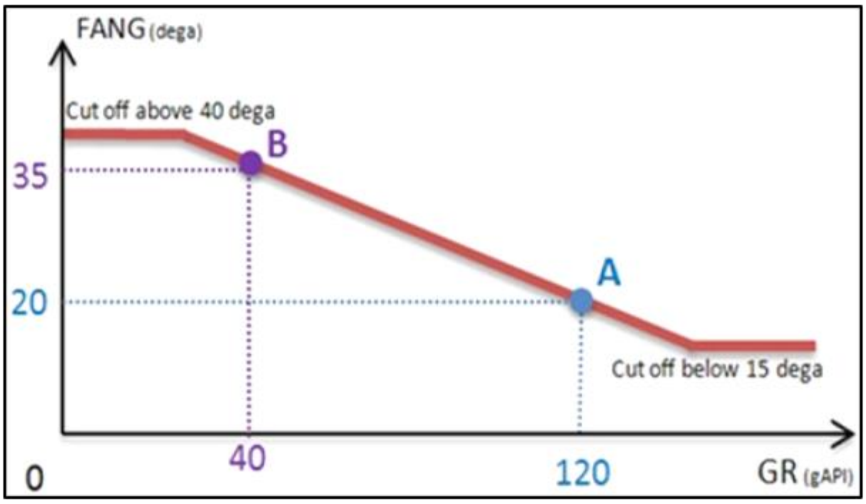

Fig. 4. Friction angle correlation using gamma ray log [45]

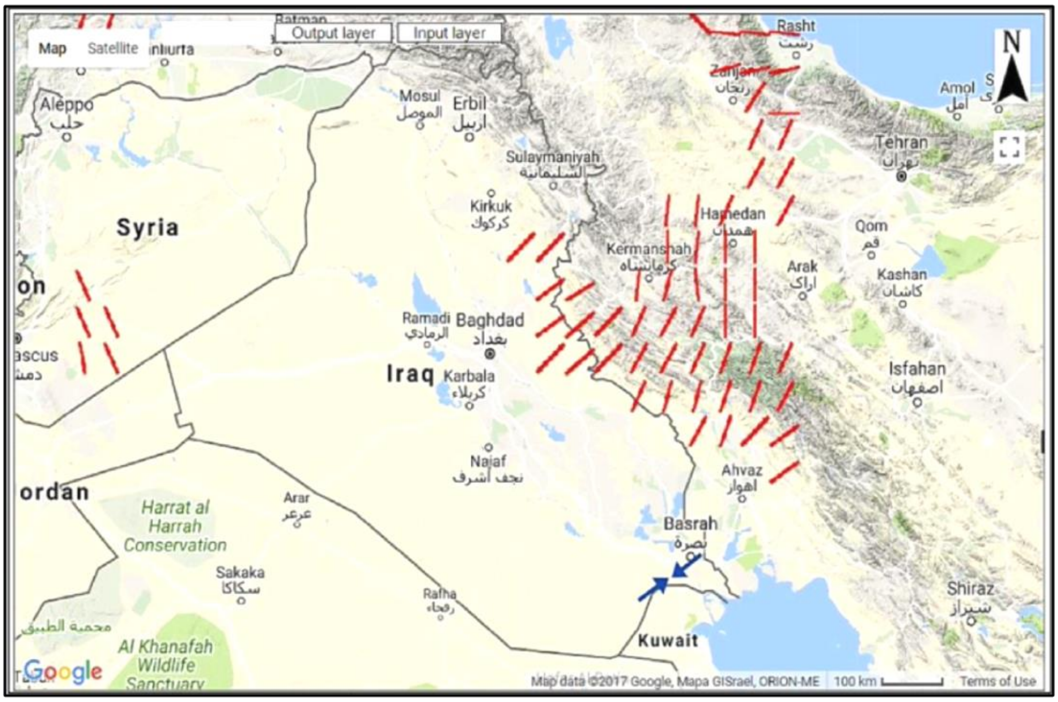

Fig. 5. Maximum possible horizontal stress in the common direction [50]

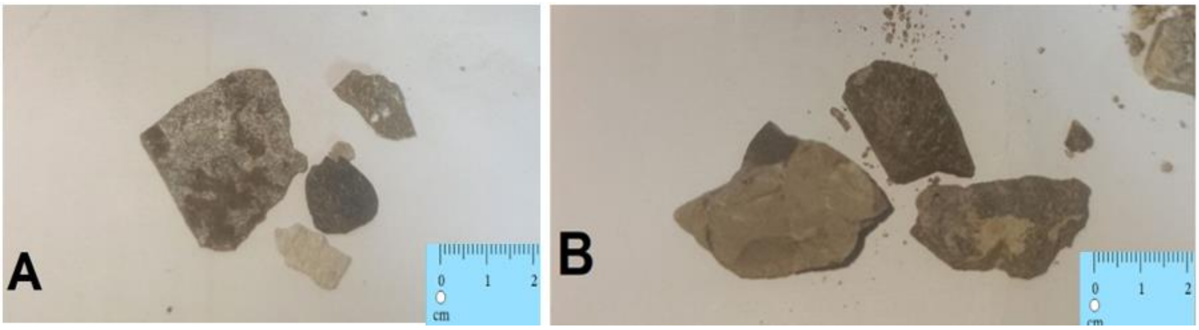

Fig. 6. Cutting samples from mauddud formation: A) well B. B) well C

3.1. Scanning electron microscopy (SEM)

3.1.1. SEM practical basis

SEM is used to examine pore networks and microstructural characteristics in geomechanical properties during testing [51], the SEM test device is shown in Fig. 7A. Examining testes samples sections help geologists identify fractures and vugs. A SEM can visualize characteristics from meters to millimeters. Crack distribution and shape in SEM images are critical for understanding rock anisotropy data and predicting mechanical characteristics [9]. The fundamental principle of the scanning electron microscope involves generating an electron beam through the establishment of a potential difference in the electron source, as shown in Fig. 7B. The beam initially traverses a condensing lens. The function of these lenses is to constrict the primary beam to a specified degree. The beam subsequently traverses a sequence of coils (wires) known as Scan Coils, which manipulate the beam's horizontal position by generating an electromagnetic force. The beam ultimately traverses the objective lens, which is responsible for concentrating the beam on the sample. Upon impact with the sample, a series of electron beams are emitted from the surface and subsequently detected by sensors positioned above the sample. The identification of the sample is achieved through the conversion of these electrons into signals [52].

3.1.2. Collection and preparation of samples for SEM analysis

Fundamental sample preparation every SEM comes with a sample container or loading chamber for sample insertion. It is advisable to utilize aluminum stubs for loading a sample in a SEM. It is essential that the sample is securely bonded to the surface of the stub prior to its placement in the sample holder or stage. Preparation of samples is advisable to eliminate any loose particles from samples. To do this, one may provide dry air to the sample by spraying [53]. Ensure to implement the subsequent precautions: 1- Avoid directing dry air towards any electronic devices or scanning electron microscopes, since it may provide a fire hazard. 2-Use care when manipulating your sample to prevent destruction. 3-Ensure that the mounting technique is stable to prevent any issues.

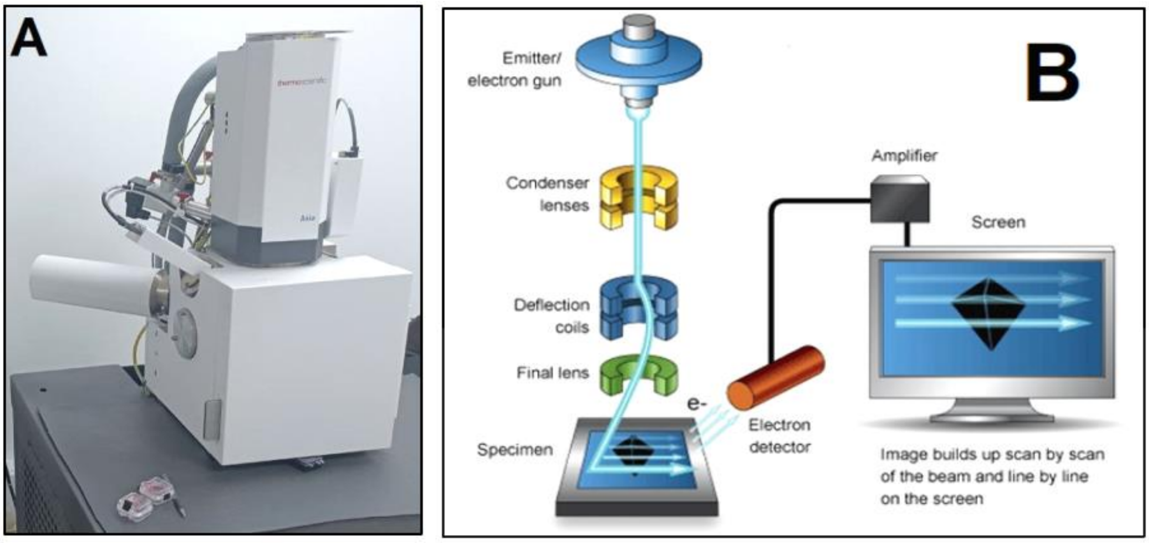

Fig. 7. A) SEM and EDS device. B) schematic of scanning electron microscope (SEM)

3.2. Energy-dispersive x-ray spectroscopy (EDS)

3.2.1. The practical basis of the energy dispersive spectroscopy EDS analysis system

The foundation of EDS analysis involves the destruction of a sample with electron beams, resulting in the displacement of some of the atom's electrons and the creation of an empty space. An electron from a higher energy level then transitions to fill this empty space, allowing the atom to achieve equilibrium. During this process, the electron relinquishes a portion of its energy, corresponding to the energy difference between the two levels. The energy is emitted as X-rays, which are distinctive to each element. Consequently, it is utilized to examine the components found in the sample, [54]. Predicting a reservoir's geomechanical behavior requires an understanding of its mineral composition as indicated by Energy Dispersive Spectroscopy (EDX) [54], the EDS test device is shown in Fig. 7A. The investigation of geomechanical properties is supported by mineralogical data. This analysis identifies the mineral causes underlying the sample's behavior and, by extension, the behavior of the reservoir. To analyze the behavior of properties under stress, the examination of rock mineralogy through EDS results was conducted, which yields weight percent mineralogy [23]. The behavior of rocks under stress is affected by their mineral composition, which relates to the mechanical properties of ductility and brittleness [55]. The results of the conducting test for the studied samples are presented in Table 2 and Table 3.

Table 2. EDS Mineralogy of Well B

Element	Weight % Error	Weight %	Atomic % Error	Atomic %
C	0.1	12.3	0.2	22.8
O	0.4	35.0	0.6	48.6
Mg	0.0	0.3	0.0	0.3
Si	0.0	1.2	0.0	0.9
Ca	0.2	47.8	0.1	26.5
Fe	0.1	0.8	0.0	0.3
Ni	0.1	0.6	0.0	0.2
Ba	0.2	2.0	0.0	0.3

Table 3. EDS mineralogy of well C

Element	Weight % Error	Weight %	Atomic % Error	Atomic %
C	0.2	12.9	0.3	22.6
O	0.6	39.6	0.8	52.0
Mg	0.1	0.5	0.1	0.4
Si	0.0	1.1	0.0	0.9
Ca	0.2	45.9	0.1	24.1

3.2.2. Preparation sample to (EDS) system analyses

The steps in preparing the sample for SEM testing are similar to those for EDS testing in terms of cleaning, drying, and other steps mentioned in the section on preparing the sample for SEM testing [53]. The main difference between the two tests is that in SEM testing, the sample must be covered with a thin layer of metal, while in EDS testing, this is not done. Also, the sample preparation requires lower atmospheric pressure than in EDS testing.

3.3. X-ray diffraction (XRD)

3.3.1. XRD practical basis

Diffraction is a phenomenon where X-rays are dispersed by atoms inside a crystal lattice in particular spatial orientations, reinforcing one another to generate more intense rays. This phenomenon is the main direct method for detecting the phase composition and structure of materials. The XRD is mostly used to detect the phase of crystalline materials and determine unit cell size. This method is commonly used to identify unknown crystalline materials, such as minerals and inorganic chemicals. X-ray diffraction methods include high-resolution investigation of heteroepitaxial layers, thin film reflectometry, and small-angle scattering [56].

3.3.2. Collection and preparation of samples for XRD analysis

The sample is first ground up into very small pieces. The goal is to get a powder that is all the same and has bits of the same size. It is then mixed with a glue, which helps the pieces stay together while they are being dried. The next step is to put the mixture into a container for grinding and then place it into a pressing cylinder. The crushing tool is chosen based on the size and shape of the pellets that are wanted. Putting pressure on the pressed disk is the next step. Depending on what tools are available, this is done with a hand press. The pellets are now solid and have a smooth surface. They are ready to be put in the XRD machine for evaluation.

The XRD test device is shown in Fig. 8A and Fig. 8B. Table 4 shows the semi-quantitative analysis obtained by X-Ray diffraction for rock samples (in Weight %).

3.4. Thin section test (TS)

Very thin materials derived from rock samples are used in this test. This test involves measuring the surface of a component, very small parts, or specific portions of the sample, as well as evaluating related microstructures. The resultant picture may be utilized to characterize rock microfacies and porous shape. This test has been performed in the present work on two samples from the Mauddud formation in two wells. The results of TS from well B, illustrated in Fig. 21, and from well C, illustrated in Fig. 22.

4- Empirical correlations

There are two ways to analyze rock mechanical characteristics. A method for assessing stress-strain behavior involves applying varying load ranges to a rock sample. This approach measures the formation's static elastic characteristics. The other technique measures compressional and shear wave propagation velocities to determine dynamic rock elastic characteristics utilizing basic relations. We will exclude samples with high clay content to decrease data mismatch and create a systematic equation for the required relationships. This section describes the major outlines for using these two methodologies in the reservoir investigation.

4.1. Relationship between compressional and shear wave velocities

Fig. 9, illustrates the linear correlation between the compressional and shear velocities of the 12 samples taken from Mauddud formation. The derived equation's high correlation coefficient (0.9007) indicates a strong connection between the two velocities. The derived Eq. 16 is shown below :

$$Dts = 1.3844\ Dtc + 25.997 \qquad (16)$$

The lack of shear slowness in typical logging data renders the experimentally developed equation useful for approximating the shear slowness of the reservoir at any depth. The derived Eq.16 can be used for any well in the studied field to obtain Dts from the conventional knowing Dtc.

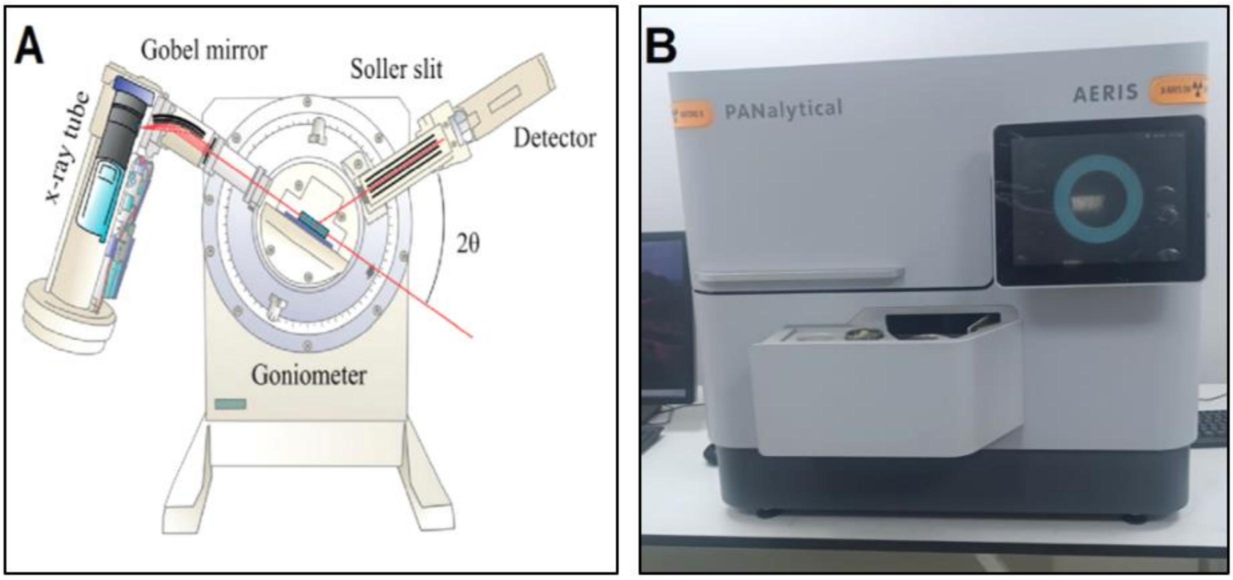

Fig. 8. A) Schematic of XRD device [57]. B) XRD device used in this study

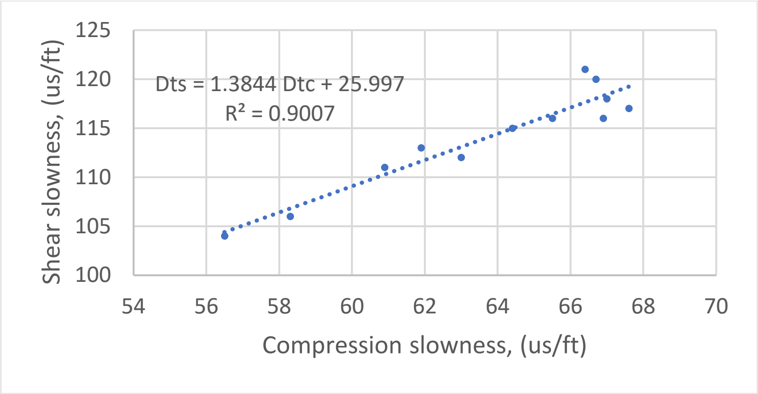

Fig. 9. Relationship between compressional and shear slowness

4.2. Getting relationships for compression strength (UCS)

Compressive strength can be determined using velocity or mechanical parameters. Fig. 10 illustrates relationship between compressional slowness and compressive strength. The derived equation's low correlation coefficient (0.2887) indicates a weak relation between them. Shear slowness data did not succeed in communicating well with the UCS, also.

Fig. 11 illustrates the correlation between compressive strength (UCS) and Young’s modulus for the examined reservoir. The data in blue color refers to relation between static young's modulus (Es) and UCS, the derived equation's low correlation coefficient (0.3415) indicates a week connection between them. While there is moderate agreement in the second relation-in orange color- between dynamic modulus (Ed) and UCS, with moderate correlation coefficient (0.556). The derived Eq.17 is shown below:

$$UCS = 3492.1\ Ed - 11302 \qquad (17)$$

It is not easy to measure compressive strength using Young's modules in practice. For this reason, the resulting connection will either emphasize or undervalue the UCS. More than 90% of the whole sample mineral, including calcite, quartz, and cement, were identified throughout the diagnostic process, which is the reason estimated UCS shows some scatter in Fig. 12. Core samples and cuttings were subjected to an X-ray diffraction (XRD) examination, which revealed the presence of these minerals.

The identical range and types of mineral content (calcite, quartz, and cement) in the core samples result in significant variability when establishing a correlation between compressive strength UCS and core porosity. Fig. 12 illustrates significant data scattering, indicating that porosity by itself may not serve as an accurate indicator for estimating compressive strength. The challenges in establishing a constructive relationship between rock compressive strength and porosity are also noted by [41]. The author observes that the majority of empirical equations concerning rock physical properties and strength are not consistent with the measured data.

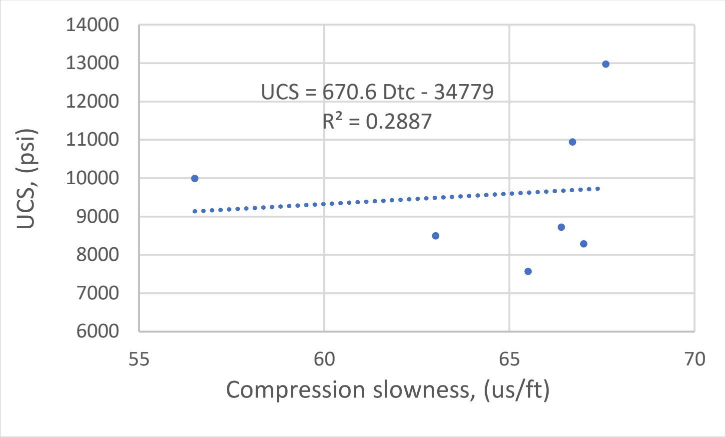

Fig. 10. Relationship between compression slowness and UCS

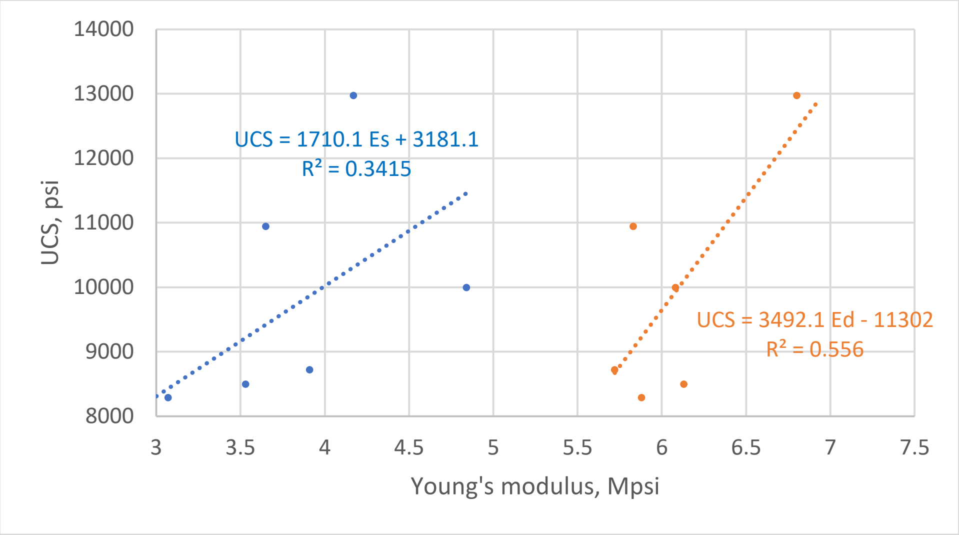

Fig. 11. Relationship between young's modulus and UCS

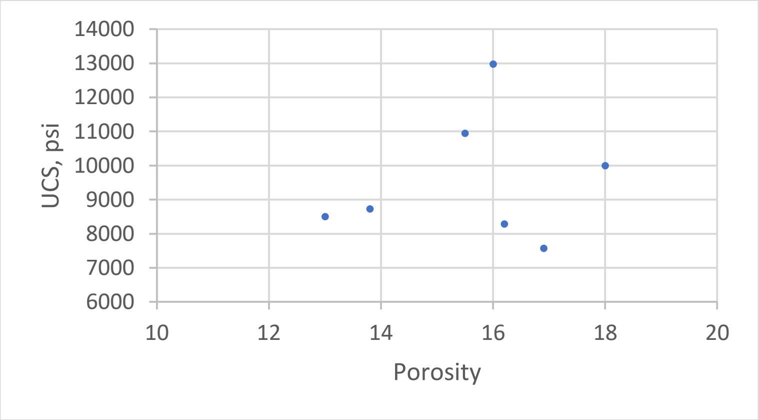

Fig. 12. Relationship between porosity and UCS

4.3. Compression and shear slowness relationship with density

The relationship between slowness and density (d) is an inverse relationship, because the wave velocity is directly proportional to the density of rocks [14]. Therefore, a direct relationship was found between slowness and the density of the Mauddud Formation in Badra Field, whether that relationship is between (Dtc) and density or (Dts) and density. Fig. 13 show that there is a medium or good relationship and correlation coefficient (0.6384) with Dtc. The derived Eq. 18 is shown below:

Dtc = - 0.0895 d + 283.91 (18)

Also, there is a moderate to good correlation coefficient (0.685) for Dts with bulk density, Fig. 14.

The derived Eq. 19 is shown below:

Dts = - 0.1353 d + 446.85 (18)

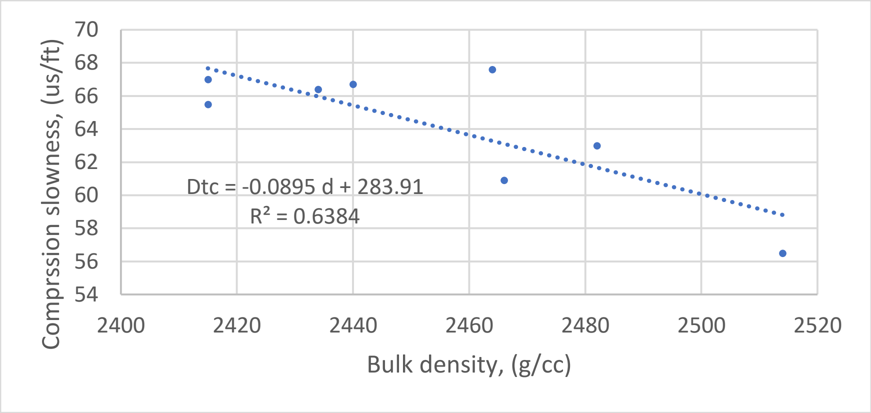

Fig. 13. Relationship between compression slowness and bulk density

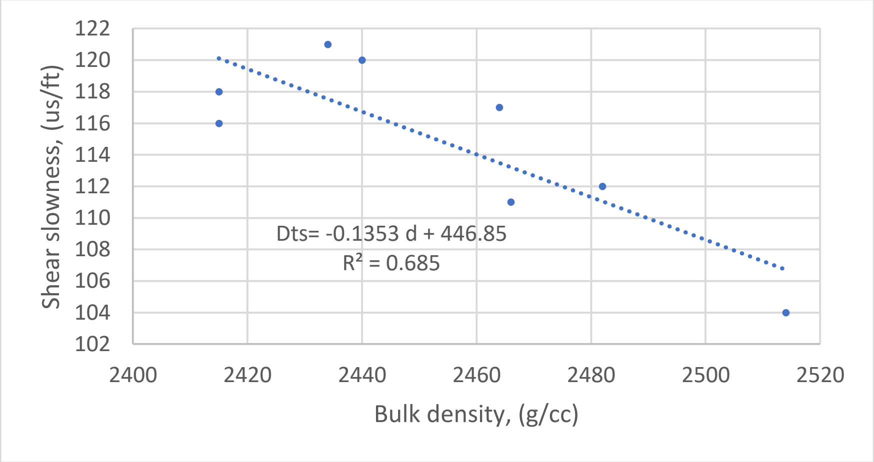

Fig. 14. Relationship between shear slowness and bulk density

5- Results and discussion

5.1. 1D MEM results

The analyses of well log data used to determine the geomechanical properties in Badra field, particularly Mauddud Formation after processing using Techlog software,[58], for two studied wells are shown in Fig. 15. This figure yielded results that were largely accurate and reliable. The results from the equations used to calculate geomechanical properties (Eq. 7 to Eq. 11) can be calibrated with those measured accurately in the laboratory. The calculated data shows consistently compatible well with the measured data.

The anode compartments in the PMDCs received a steady inflow of real household wastewater at a rate of 1.04 ml/min, facilitated by an adjustable peristaltic pump. Concurrently, the desalination chambers in the PMDCs were provided with a synthetic saline solution at a flow rate of 0.5 ml/min, utilizing a peristaltic pump (BT100S, GOLANDER PUMP, USA). Inoculation of mixed biomass and microalgae was carried out in the anode and cathode chambers, respectively.

According to Fig. 15 the Young's modulus of the Mauddud Formation, designated as (YME_STA_JFC) in the third track, calculated using Eq. 9, shows that 4 MPa being the most prevalent value throughout the formation. Poisson's ratio (PR_STA), calculated using Eq. 10, indicated the value of 0.27 was identified as the most prevalent, aligning with Poisson's ratio values of carbonate reservoirs found in the Mauddud Formation. Rzhevsky and Novick Carbonate Porosity Correlation was used to find the UCS using Techlog software in track three and is indicated by the symbol (UCS_CAR_RNC). The calculated results were found to be matched well with the measured data shown in red color and indicated by the symbol (UCS) in the same track.

The friction angle, designated as (FANG_FromGr), was determined through using gamma ray log, in the second track, resulting in values ranging from 36 to 38 degrees, consistent with laboratory measurements. To find the tensile strength (TSTR) as shown in the second track, calculated using Eq. 11, the median value was found to be

1300 psi, the rocks typically include tiny fissures, which are the primary source of the fractured rocks following tensile failure. The presence of fissures contributes to tensile failure upon attaining maximum stress.

Analysis of stress results in the fourth track of Fig. 15, for well B, revealed that the pore pressure, denoted as PPRS_EATON_S, calculated by Eq. 5, was generally normal across most regions, with exceptions noted in specific zones, especially in Mauddud D at 4610m depth. This unusual result corresponds with an increase in fracture pressure (FPRS_EARON) in the same locations, calculated using Eq. 6, thus explaining a small probability of fracturing within this layer. The recorded results for horizontal stresses, both maximum (SHMAX_PHS), calculated by Eq. 12, and minimum (SHMIN_PHS), calculated by Eq. 13, were relatively large, but they are smaller than vertical stress (SVERTICAL_EXT) typically, calculated by Eq. 1.

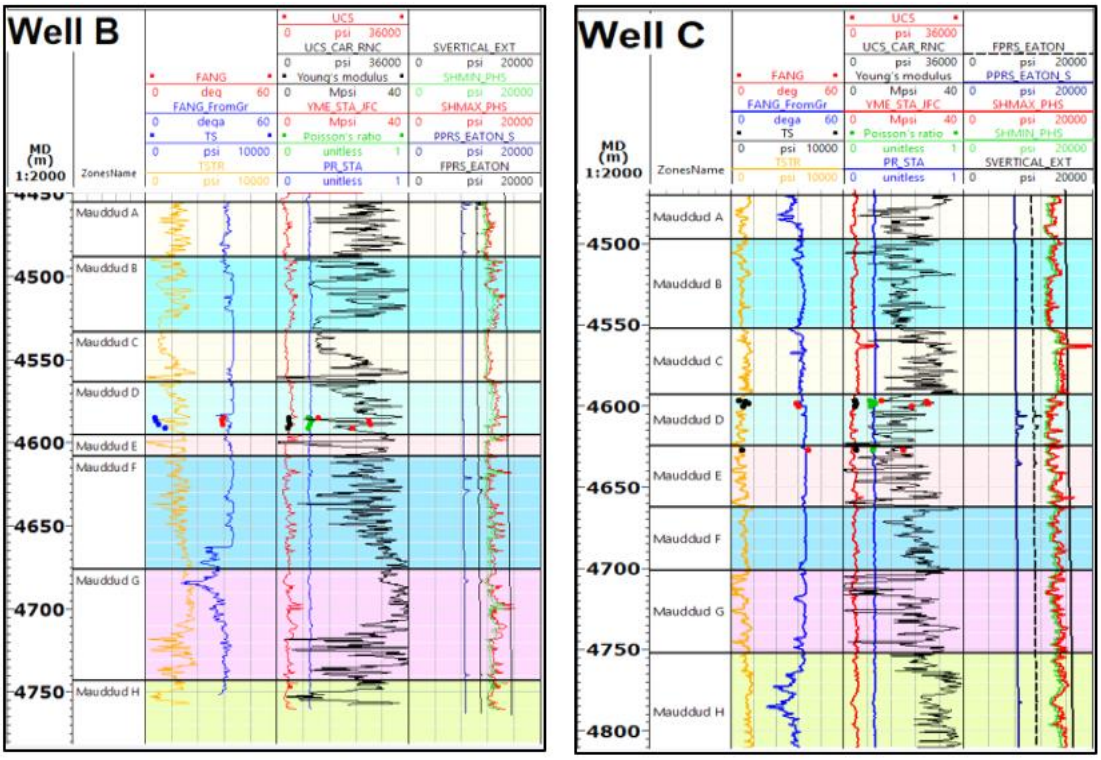

Fig. 15. Components of 1-D-MEM results with measured data. A) well B, B) well C

5.2. UCS results

UCS is very important property that expresses rock strength to fracability, therefore selecting appropriate correlation to accurately estimate UCS is an important step. The chosen correct correlation will be used in subsequent steps of MEM modeling constructing. To do this step in this study, the six correlations mentioned previously in Table 2 were tested for accuracy using measured data and the calculation results are illustrated in Fig. 16. Fig. 16, shows unconfined compressive strength results after using six correlations mentioned previously in Table 2. For Eq. 1 and Eq. 3 in Table 2, they are limited to reservoirs with porosity between approximately 0.05 and 0.2, which is a narrow range for the formation under study. Therefore, there was no significant agreement between the results of these equations and the field measured data. For Eq. 2 in Table 2, which obviously relies on porosity as input data, the results from this equation were the best and a good agreement between Rzhevsky and Novick Carbonate Porosity Correlation (Eq. 2 in Table 2) with laboratory test data compared to other correlations are obtained. This is due to the fact that the rock mechanical properties in the Korobcheyev deposit are somewhat similar to those in the Mauddud Formation. Referring to Eq. 4 in Table 2, it contains two variables: porosity and sonic transit time. Due to the rock hardness in the Mauddud Formation, which reaches 200 Mpa, this equation results in lower values than those measured, because it applies to reservoirs with average UCS of (40-160) Mpa. Eq.5 and Eq.6 in Table 2 are utilized, both of which are designed to predict the unconfined compressive strength (UCS) of carbonate rock in different worldwide locations, but they are clearly underestimate rock strength.

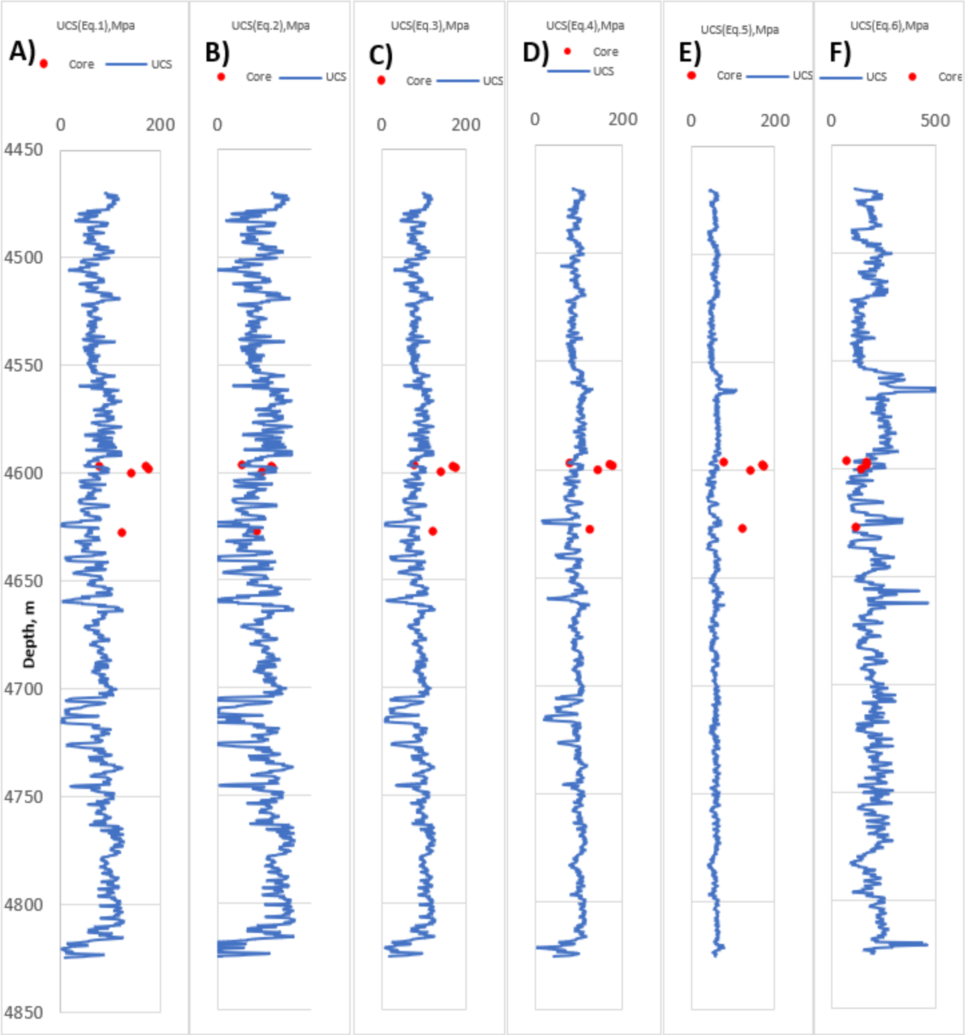

Fig. 16. Unconfined compressive strength measured by numerous published correlations which were mentioned in Table 1, A) Eq. 1, B) Eq. 2, C) Eq. 3, D) Eq. 4, E) Eq. 5, F) Eq. 6

5.3. Experimental rock evaluation results

5.3.1. SEM results

SEM images are shown in Fig. 17 and Fig. 18, images for sample microstructures highlight essential factors that affect rock strength. Fig. 19 and Fig. 20; display the results of well B and well C, respectively, in this article. Microcrystalline limestone is densely packed in the samples. The rock's strength and stiffness are greatly enhanced by these coarse grains, making it more resistant to open cracks. Pores and vugs occur in microcrystalline areas. The "normal trend" in the stress-permeability connection can be better understood by looking at the microcrystalline structure as a whole.

5.3.2. XRD results

Table 4 shows the semi-quantitative analysis obtained by X-Ray diffraction for rock samples (in Weight %). According to the XRD test, calcite is the most common mineral in the sample, where 95% of the weight of the sample was recorded as calcite. This mineral represents the largest percentage in the composition of carbonate reservoirs to which the Mauddud formation belongs. Total clay up to 5% of total mineral content (Kaolinite and Illite), making it the second mineral percentage after calcite. Quartz, on the other hand, up to 3% of the total mineral composition in the samples that were considered. Core porosity and log data accuracy are both affected by the concentration of these minerals in the samples.

The width of the peaks is inversely proportional to the size of the crystal, as shown in Fig. 19 and Fig. 20 The thinner the top, the larger the crystal. The wider the top, the smaller the crystal, the defect in the crystal structure, the inherently amorphous the sample, or a solid that lacks crystallization. Thus, given the width of the peaks in Fig. 19 for well B, and Fig. 20 for well C, they indicate the presence of large crystals of calcite. In a similar XRD analysis study conducted by [59] on Quartz-Hematite and Quartz-Magnetite samples, the results showed through the mineral peaks of the QHB sample that there is a high percentage of hematite (2.70 Å), while for the second model QMB the results showed a low percentage of hematite (1.48 Å).

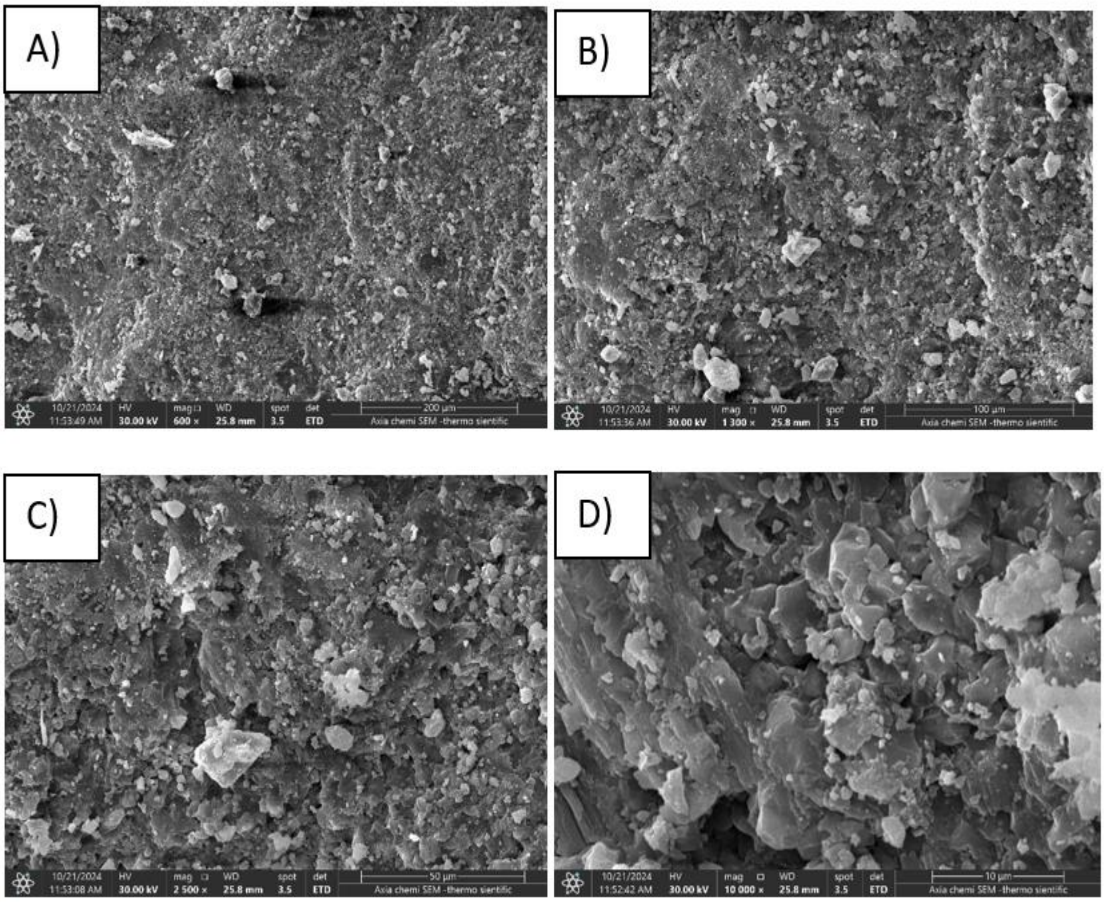

Fig. 17. SEM Images of cutting sample from well B, A) ×600, B) ×1300, C) ×2500 D) ×10000

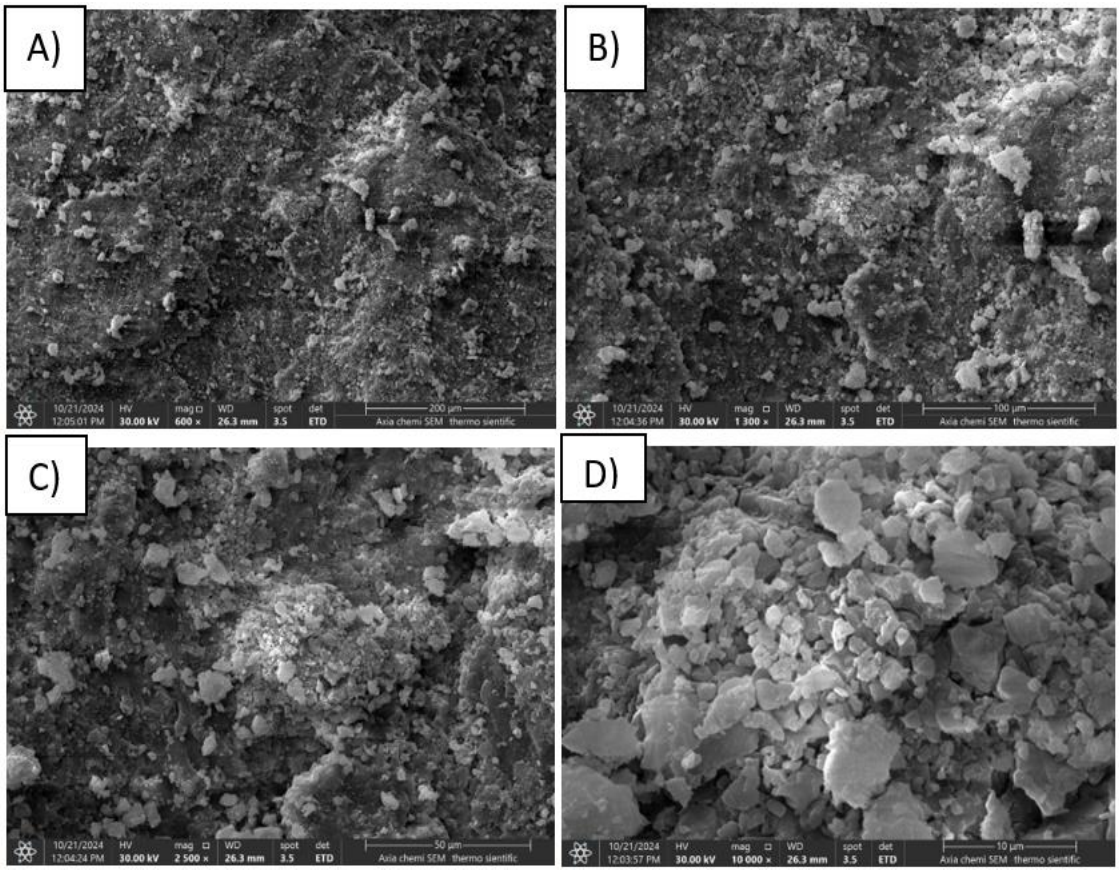

Fig. 18. SEM Images of cutting sample from well C, A) ×600, B) ×1300, C) ×2500 D) ×10000

Table 4. Semi-quantitative analysis obtained by x-ray diffraction

Well name	Depth(m)	Formation	Mineralogical Composition (wt%)				Total (wt %)
			Illite	Kaolinite	Quartz	Calcite	
B	4518	Mauddud B	2.25	1.96	-	95.79	100.00
C	4593	Mauddud D	-	-	2.90	97.10	100.00

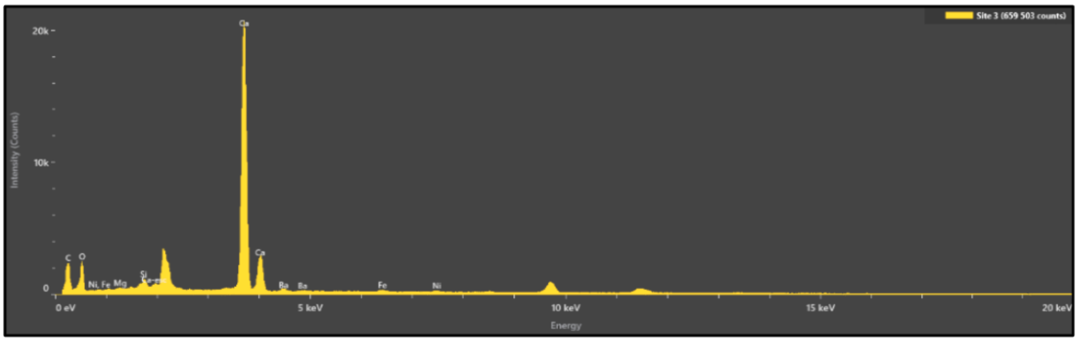

Fig. 19. XRD patterns result for well B

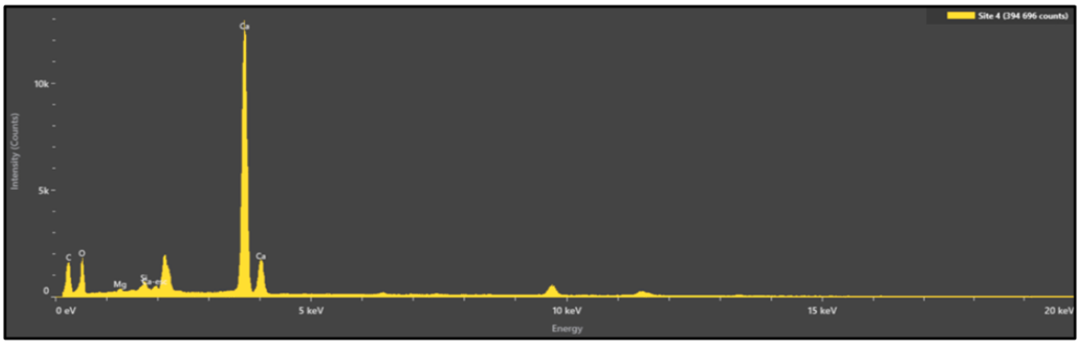

Fig. 20. XRD patterns result for well C

5.3.3. Thin section (TS) results

Fig. 21, illustrates Thin Section image of cutting sample of well B, the skeletal grains [common amount of benthic foraminifera (B), few amounts of pelecypod shell fragments (Pe), as well as rare amounts of gastropods, echinoderm plates (E), ostracods, crustose coralline red algae and calcispheres], and non-skeletal grains [very few amount of peloids (P)], there are frequent amount of micritic/microsparitic matrix (Mi), and common amount of blocky non-ferroan calcite cement (C), minor amount of non-ferroan dolomite rhombs (D), Rare amounts of black pyrite crystals and residual hydrocarbons, as well as, traces of fluorite and hydrocarbon stains. Porosity type of this sample is fracture porosity with very poor pore interconnectivity.

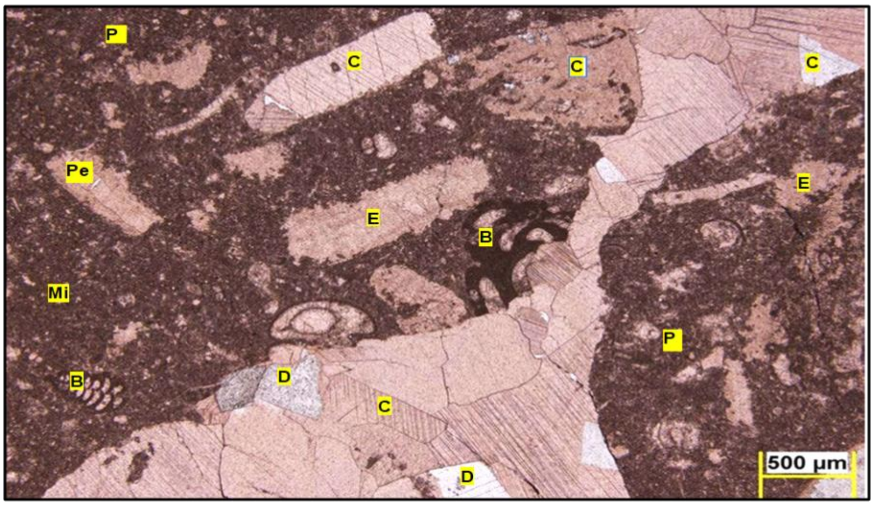

Fig. 21. Thin section image of cutting sample of well B

Fig. 22, illustrates Thin Section image of cutting sample of well C, the skeletal grains [dominant amount of benthic foraminifera (B; mainly Orbitolinids), very few amounts of echinoderm plates (E), pelecypod shell fragments (Pe) and crustose coralline red algae (Al), rare amount of calcispheres and bryozoan fragments], and non-skeletal grains [common amount of peloids (P), in addition to, rare amount of cortoids], there are minor amount of non-ferroan sparry calcite cement (C), rare amounts of non-ferroan dolomite rhombs and residual hydrocarbons, as well as, traces of fluorite crystals, pyrite and hydrocarbon stains. Porosity type of this sample is intragranular, moldic and fracture pore types (orange arrows), with moderate pore interconnectivity.

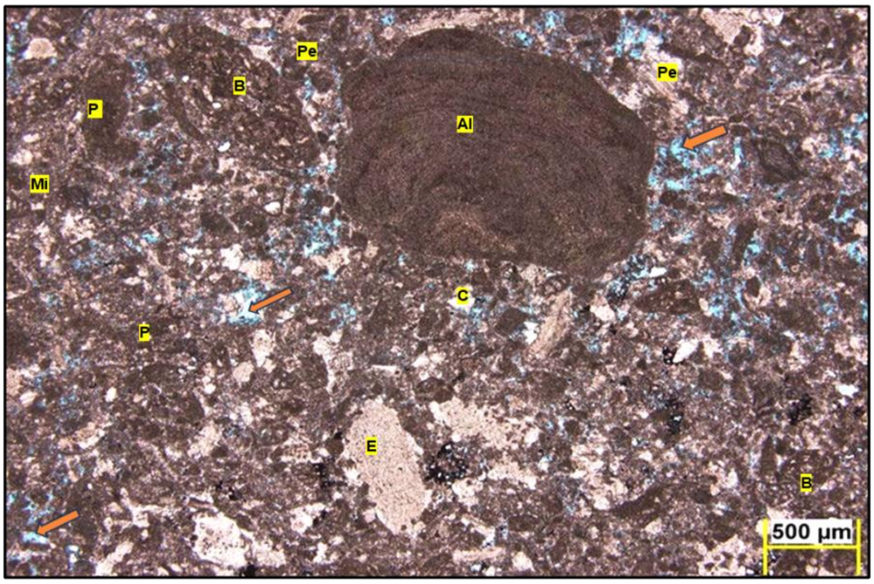

Fig. 22. Thin section image of cutting sample of well C

6- Conclusion

This study integrates Laboratory investigation and calibrated 1D MEM to investigate the geomechanical characteristics of the Mauddud Formation in the Badra Oil Field. Detailed analyses using SEM, XRD, EDS and TS have improved the understanding of the behavior and strength of carbonate rock strength and deformation characteristics. The subsequent conclusions are derived from the outcomes of constructing a 1-D Mechanical Earth Model and laboratory tests results:

1- Distinct correlation has been obtained between UCS and Young's Modulus; however, this correlation is significantly influenced by whether the modulus is static or dynamic, underscoring the necessity of selecting the appropriate testing methodology to ascertain the geomechanical properties of rocks.

2- Mineralogy composition of the carbonate rocks significantly influences the compressive strength and flexible characteristics of the Mauddud Formation. XRD analysis verifies the predominance of calcite with a robust crystalline structure, corroborated by EDS data indicating elevated levels of calcium and carbon. Thin section (TS) examination precisely validates these findings, indicating a substantial proportion of calcite that enhances the mechanical strength of the formation rocks.

3- Low porosity values obtained from well data and SEM imaging align with the elevated UCS values and Young's modulus. The existence of little microcracks further substantiates the structural strength of the formation.

4- No definitive porosity and UCS trends emerge, as laboratory measurements for both variables exhibit scatter driven by mineralogical heterogeneity. Thin section (TS) analysis demonstrates distinct variations in porosity between the two samples that studied.

Nomenclature

Symbol	Name	Unit
d	Bulk density	g/cc
Dtc	Compression slowness	us/ft
Kdyn	dynamic bulk modulus	Mpsi
Gdyn	dynamic shear modulus	Mpsi
Edyn	dynamic Young's modulus	Mpsi
σ^{-}	effective stress	psi
Pf	fracture pressure	psi
FANG	Friction angle	degree
Ppn	hydrostatic pore pressure	psi
σH	Maximum horizontal stress	psi
σh	Minimum horizontal stress	psi
V	Poisson's ratio	Unitless
Pp	Pore pressure	psi
Dts	Shear slowness	us/ft
TS	Tensile strength	psi
UCS	Unconfined Compressive Strength	psi
σv	Vertical Stress	psi

References

[1] N. Cross et al., "Reservoir description of a mid-Cretaceous siliciclastic-carbonate ramp reservoir: Mauddud Formation in the Raudhatain and Sabiriyah fields, North Kuwait," *GeoArabia*, vol. 15, no. 2, pp. 17–50, 2010, https://doi.org/10.2113/geoarabia150217

[2] F. N. Sadooni and A. S. Alsharhan, "Stratigraphy, microfacies, and petroleum potential of the Mauddud Formation (Albian–Cenomanian) in the Arabian Gulf basin," *AAPG Bulletin*., vol. 87, no. 10, pp. 1653–1680, Oct. 2003, https://doi.org/10.1306/04220301111

[3] W. G. AL-mutury, R. A. AL-Muhammad, and K. Al-Bayatee, "Tectonostratigraphy of Lower Cretaceous in Southern Iraq," *Iraqi National Journal of Earth Science*, vol. 10, no. 2, pp. 29–44, 2010.

[4] M. J. Faisal and T. A. Mahdi, "Geological model of Mauddud Formation in Badra Oilfield," *The Iraqi Geological Journal*, pp. 58–67, 2020, https://doi.org/10.46717/igj.53.1a.R4.2020.01.28

[5] I. Ghafor, A. Fatah, and A. A. L. Khafaf, "Biostratigraphy and Microfacies of the Mauddud Formation (Late Albian–Early Cenomanian) in Musaiyib Well No. 1, Central Iraq," *Iraqi Bulletin of Geology and Mining*, vol. 19, no. 2, pp. 37–56, 2023, https://doi.org/10.59150/ibgm1902a03

[6] K. A. Kareem, "OPTIMIZATION OF WATER INJECTION FOR BADRA OIL FIELD," vol. 53, no. 1, pp. 13–28, 2020, *The Iraqi Geological Journal*, https://doi.org/10.46717/igj.53.1B.2Rz-2020-03-02

[7] S. Z. Jassim and J. C. Goff, Geology of Iraq. DOLIN, sro, distributed by *Geological Society of London*, 2006.

[8] M. J. Faisal and T. A. Mahdi, "Diagenetic processes overprint and pore types of Mauddud formation, Badra oil field, Central Iraq," *Iraqi Journal of Science*., vol. 61, no. 6, pp. 1353–1361, 2020, https://doi.org/10.24996/ijs.2020.61.6.13

[9] N. Jasim, S. M. Hamd-Allah, and H. Abass, "Evaluation of geomechanical properties for tight reservoir using uniaxial compressive test, ultrasonic test, and well logs data," *Petroleum and Coal*, vol. 62, no. 2, pp. 329–340, 2020.

[10] A. Mockovciakova and B. Pandula, "Study of the relation between the static and dynamic moduli of rocks," *Metalurgija*, vol. 42, no. 1, pp. 37–39, 2003.

[11] W. Fei, B. Huiyuan, Y. Jun, and Z. Yonghao, "Correlation of dynamic and static elastic parameters of rock," *Journal of Geotechnical Engineering*, vol. 21, no. 04, pp. 1551–1560, 2016.

[12] M. Salah, A. Abdel-Meguid, B. Crane, S. Squires, and L. Matzar, "Geomechanical Evaluation Enabled Stimulation Optimization of Apollonia Tight Chalk Egypt," in *SPWLA Annual Logging Symposium*, 2017.

[13] M. K. Bandara and N. J. Al-Ameri, "Wellbore Instability Analysis to Determine the Safe Mud Weight Window for Deep Well, Halfaya Oilfield," *Iraqi Geological Journal*, vol. 57, no. 1D, pp. 153–173, 2024, https://doi.org/10.46717/igj.57.1D.13ms-2024-4-23

[14] A. F. Zaidan, F. A. Hadi, and M. Klempa, "Investigation of Wellbore Instability in Southern Rumaila Oil Field" *Iraqi Journal of Chemical and Petroleum Engineering*, vol. 25, no. 2, pp. 17–31, 2024, https://doi.org/10.31699/IJCPE.2024.2.2

[15] A. K. Abbas, H. H. Dahm, R. E. Flori, and M. Alsaba, "Laboratory Measurements of Petrophysical and Geomechanical Properties for Zubair Sandstone Formation in Southern Iraq," in *ARMA US Rock Mechanics/Geomechanics Symposium*, p. ARMA-2018.

[16] B. Nagham Jasim Fayadh and S. M. Hamd-Allah Hazim H Abass, "Implication of Geomechanical Evaluation on Tight Reservoir Development / Sadi Reservoir Halfaya Oil Field." the Requirements for The Degree of Doctorate of Philosophy in Petroleum Engineering University of Baghdad. 2020, http://dx.doi.org/10.13140/RG.2.2.13608.80640

[17] H. S. A. Almalikee, "Mechanical Earth Model (1D) to optimize high angle wells design in Rumaila oilfield, Southern Iraq," Collage of Science University of Basrah, pp. 3–4, 2020.

[18] J. P. Davies and D. K. Davies, "Stress-dependent permeability: characterization and modeling," *SPE Annual Technical Conference and Exhibition*, vol. 6, no. 02, pp. 224–235, 2001. https://doi.org/10.2118/71750-PA

[19] H. King et al., "Microstructural investigation of stress-dependent permeability in tight-oil rocks," *Petrophysics*, vol. 59, no. 01, pp. 35–43, 2018.

[20] G. Muktadir, M. Amro, N. Kummer, C. Freese, and K. Abid, "Application of x-ray diffraction (Xrd) and rock–eval analysis for the evaluation of middle eastern petroleum source rock," *Energies*, vol. 14, no. 20, p. 6672, 2021. https://doi.org/10.3390/en14206672

[21] V. Kumar, C. H. Sondergeld, and C. S. Rai, "Nano to macro mechanical characterization of shale," in SPE Annual Technical Conference and Exhibition, SPE, 2012, p. SPE-159804. https://doi.org/10.2118/159804-MS

[22] J. Mason, J. Carloni, A. Zehnder, S. P. Baker, and T. Jordan, "Dependence of micro-mechanical properties on lithofacies: Indentation experiments on Marcellus shale," in *SPE/AAPG/SEG Unconventional Resources Technology Conference*, URTEC, 2014, p. URTEC-1922919. https://doi.org/10.15530/URTEC-2014-1922919

[23] H. Yu, W. Zheng, X. Cui, and J. Zhou, “Influence of Mineralogical Characteristics on Mechanical Properties of Montney Tight Formations Using Instrumented Indentation Test and SEM–EDS Analysis,” *Rock Mechanics and Rock Engineering*, vol. 57, no. 10, pp. 8777–8794, 2024, https://doi.org/10.1007/s00603-024-04004-3

[24] R. Plumb, S. Edwards, G. Pidcock, D. Lee, and B. Stacey, “The mechanical earth model concept and its application to high-risk well construction projects,” in *SPE/IADC Drilling Conference and Exhibition*, SPE, 2000, p. SPE-59128. https://doi.org/10.2118/59128-MS

[25] M. Aman, D. N. Espinoza, A. G. Ilgen, J. R. Major, P. Eichhubl, and T. A. Dewers, “CO2-induced chemo-mechanical alteration in reservoir rocks assessed via batch reaction experiments and scratch testing,” *Greenhouse Gases: Science and Technology*, vol. 8, no. 1, pp. 133–149, 2018, https://doi.org/10.1002/ghg.1726

[26] A. Ihsan, N. Jasim, and A.- Ameri, “Identifying the high potential zones for hydraulic fracture propagation / Eastern Baghdad field,” *Iraqi Journal of Chemical and Petroleum Engineering*, vol. 25, no. 3, pp. 135–151, 2024. https://doi.org/10.31699/IJCPE.2024.3.15

[27] A. K. AlHusseini and S. M. Hamed-Allah, “Estimation Pore and Fracture Pressure Based on Log Data; Case Study: Mishrif Formation/Buzurgan Oilfield at Iraq,” *Iraqi Journal of Chemical and Petroleum Engineering*, vol. 24, no. 1, pp. 65–78, 2023, https://doi.org/10.31699/ijcpe.2023.1.8

[28] J. J. Zhang “Applied Petroleum Geomechanics”. 2020. https://doi.org/10.1016/C2017-0-01969-9

[29] D. Hettiaratchi, “Theoretical soil mechanics and implement design,” *Soil and Tillage Research*, vol. 11, no. 3–4, pp. 325–347, 1988, https://doi.org/10.1016/0167-1987(88)90005-0

[30] Z. U. G, “An overview of pore pressure prediction using seismically derived velocities,” *Geology and Mining Research*, vol. 7, no. 4, pp. 31–40, 2015, https://doi.org/10.5897/JGMR15.0218

[31] B. A. Eaton, “The equation for geopressured prediction from well logs,” in *SPE Annual Technical Conference and Exhibition*, SPE, 1975, p. SPE--5544. https://doi.org/10.2118/5544-MS

[32] K. Terzaghi, Theoretical soil mechanics. 1943.

[33] J. Zhang, “Pore pressure prediction from well logs: Methods, modifications, and new approaches,” *Earth-Science Reviews*, vol. 108, no. 1–2, pp. 50–63, 2011. https://doi.org/10.1016/j.earscirev.2011.06.001

[34] B. A. Eaton, “Fracture gradient prediction and its application in oilfield operations,” *Journal of Petroleum Technology*, vol. 21, no. 10, pp. 1353–1360, 1969, https://doi.org/10.2118/2163-PA

[35] P. A. Charlez, “The concept of mud weight window applied to complex drilling,” in *SPE Annual Technical Conference and Exhibition*, SPE, 1999, p. SPE-56758. https://doi.org/10.2118/56758-MS

[36] A. R. Najibi, M. Ghafoori, G. R. Lashkaripour, and M. R. Asef, “Reservoir geomechanical modeling: In-situ stress, pore pressure, and mud design,” *Journal of Petroleum Science and Engineering*, 2017, https://doi.org/10.1016/j.petrol.2017.01.045

[37] A. M. Abdulaziz, H. L. Abdulridha, A. S. A. Dahab, S. Alhussainy, and A. K. Abbas, “3D mechanical earth model for optimized wellbore stability, a case study from South of Iraq,” *Journal of Petroleum Exploration and Production Technology*, vol. 11, no. 9, pp. 3409–3420, 2021. https://doi.org/10.1007/s13202-021-01255-6

[38] R. H. Allawi and M. S. Al-Jawad, “Wellbore instability management using geomechanical modeling and wellbore stability analysis for Zubair shale formation in Southern Iraq,” *Journal of Petroleum Exploration and Production Technology*, vol. 11, pp. 4047–4062, 2021. https://doi.org/10.1007/s13202-021-01279-y

[39] H. Xu et al., “Characterization of rock mechanical properties using lab tests and numerical interpretation model of well logs,” *Mathematical Problems in Engineering*, vol. 2016, no. 1, p. 5967159, 2016. http://dx.doi.org/10.1155/2016/5967159

[40] F. H. Alshibli and A. A. Alhaleem, “Using One-Dimensional Geomechanical Model for Determining the Safe Wellbore Orientation of Zubair Reservoir, Southern Iraq,” *The Iraqi Geological Journal*, vol. 56, no. 2, pp. 115–134, 2023, https://doi.org/10.46717/igj.56.2C.9ms-2023-9-15

[41] C. Chang, M. D. Zoback, and A. Khaksar, “Empirical relations between rock strength and physical properties in sedimentary rocks,” *Journal of Petroleum Science and Engineering*, vol. 51, no. 3–4, pp. 223–237, 2006, https://doi.org/10.1016/j.petrol.2006.01.003

[42] A. Amani and K. Shahbazi, “Prediction of Rock Strength using Drilling Data and Sonic Logs,” *International Journal of Computer Applications*, vol. 81, no. 2, pp. 5–10, 2013, https://doi.org/10.5120/13982-1986

[43] “Schlumberger,” Limited. Techlog 2015.3 User Guide. *Schlumberger software*, 2015.

[44] C. Chang, M. D. Zoback, and A. Khaksar, “Empirical relations between rock strength and physical properties in sedimentary rocks,” *Journal of Petroleum Science and Engineering*, vol. 51, no. 3–4, pp. 223–237, 2006. https://doi.org/10.1016/j.petrol.2006.01.003

[45] A. S. Dahab, A. M. Abdulaziz, A. Manhalawi, A. K. Abbas, and N. AL-Husseini, “Managing wellbore instability through geomechanical modeling and wellbore stability analysis,” 54th, *U.S. Rock Mechanics / Geomechanics Symposium*, no. December 2020.

[46] M. D. Zoback et al., “Determination of stress orientation and magnitude in deep wells,” *International Journal of Rock Mechanics and Mining Sciences*, vol. 40, no. 7–8, pp. 1049–1076, 2003, https://doi.org/10.1016/j.ijrmms.2003.07.001

[47] D. Moos and M. D. Zoback, “Utilization of observations of wellbore failure to constrain the orientation and magnitude of crustal stresses: application to continental, Deep Sea Drilling Project, and Ocean Drilling Program boreholes,” *Journal of Geophysical Research: Solid Earth*, Res. Solid Earth, vol. 95, no. B6, pp. 9305–9325, 1990. https://doi.org/10.1029/JB095iB06p09305

[48] M. M. C. Carafa, G. Tarabusi, and V. Kastelic, “SHINE: Web application for determining the horizontal stress orientation,” *Computers & Geosciences*, vol. 74, pp. 39–49, 2015. https://doi.org/10.1016/j.cageo.2014.10.001

[49] N. Ural, “The significance of scanning electron microscopy (SEM) analysis on the microstructure of improved clay: An overview,” *Open Geosciences*, vol. 13, no. 1, pp. 197–218, 2021. https://doi.org/10.1515/geo-2020-0145

[50] K. Akhtar, S. A. Khan, S. B. Khan, and A. M. Asiri, “Scanning electron microscopy: Principle and applications in nanomaterials characterization”. *Springer*, 2018. https://doi.org/10.1007/978-3-319-92955-2_4

[51] P. Echlin, “Handbook of sample preparation for scanning electron microscopy and X-ray microanalysis” *Springer Science & Business Media*, 2011.

[52] D. S. Su, B. Zhang, and R. Schlögl, “Electron Microscopy of Solid Catalysts- Transforming from a Challenge to a Toolbox,” *Chemical Reviews*, vol. 115, no. 8, pp. 2818–2882, 2015. https://doi.org/10.1021/cr500084c

[53] N. J. Al-Ameri, S. M. Hamd-Allah, and H. H. Abass, “Investigating geomechanical considerations on suitable layer selection for hydraulically fractured horizontal wells placement in tight reservoirs,” in *Abu Dhabi International Petroleum Exhibition and Conference*, *SPE*, 2020, p.D012S116R166. https://doi.org/10.2118/203249-MS

[54] M. Ermrich and D. Opper, “X-Ray powder diffraction” *XRD for The Analyst*, pp. 63–85, 2011.

[55] B. S. Saini and R. Kaur, “X-ray diffraction,” Handb. Mod. Coat. Technol. Adv. Charact. Methods, pp. 85–141, 2021, https://doi.org/10.1016/B978-0-444-63239-5.00003-2

[56] *Schlumberger*, “Techlog Technical Manual,” 2015.

[57] R. Edjo-Minko, I. B. M. Gbambie, M. Vasconcelos, J. M. A. Essi, M. Amar, and M. F. M. Essi, “3D depth estimation of Mingo’o’s iron mineralization from outcrop data and geophysical analysis (South Cameroon, northern edge of the Congo Craton),” *Brazilian Journal of Geology*, vol. 54, no. 2, p. e20240020, 2024. https://doi.org/10.1590/2317-4889202420240020

تقييم الخواص الجيوميكانيكية لتكوين مودود بناءً على القياسات التجريبية وبيانات سجل الآبار

محمد المجاهد فاروق الجميلي [١، *]، نغم جاسم العامري [١]

١ قسم هندسة النفط، كلية الهندسة، جامعة بغداد، بغداد، العراق

الخلاصة

يعد تكوين مودود من ابرزالتكوينات في شمال شرق العراق نظرا لمل يمتتلكه من مخزون كبير من الهيدروكربونات الضخمة الموجودة في المكمن , مما يجعل التوصيف الجيوميكانيكي الدقيق امرا ضروريا لضمان سلامة عمليات الحفر وتوفير أساس سليم لتخطيط التنمية المستقبلية. تبنِي هذه الدراسة نموذج الأرض الميكانيكي أحادي البعد (1D-MEM) المعاير بعد الحفر لعدد من الآبار المختارة، باستخدام برنامج Techlog لدمج بيانات الخصائص الميكانيكية للصخور وسجلات الصور وقياسات جهاز المعايرة متعدد الأذرع والسجلات الباطنية التقليدية وتقارير الحفر وتحليلات عينات اللب. تقدّم منهجية الدراسة سير عمل مفصّلًا لتقدير الخصائص الجيوميكانيكية انطلاقًا من تحليل السجلات والصور وصولًا إلى معايرة النموذج، وتم التحقق من صحة موديل ١D-MEM عبر مقارنة نتائج المحاكاة بالقياسات المباشرة لضمان موثوقية توزيع الإجهادات وقيم المقاومة المتوقعة. كما استُخدمت بيانات مختبرية وميدانية متنوعة، تشمل قياسات الضغط المسامي بطريقة اختبار ساق البئر (DST)، والاختبارات الميكانيكية التدميرية وغير التدميرية، والمجهر الإلكتروني الماسح (SEM)، وفحص الشريحة الرقيقة (TS)، واختبار حيود الأشعة السينية (XRD)، ومطيافية الأشعة السينية المشتّتة للطاقة (EDS)، في عمليات التحليل والمعايرة. تُسهم هذه البيانات في تحسين معايير موديل الأرض الميكانيكي ودعم اشتقاق علاقات تجريبية خاصة بتكوين مودود، تشمل علاقات بين بطء الموجات الانضغاطية والقصية، وعلاقات بين بطء الموجات والكثافة الكلية، وعلاقة بطء الموجات الانضغاطية بمقاومة الضغط غير المحصور (UCS)، والعلاقة بين معامل يونغ ومقاومة الضغط غير المحصور. تُظهر النتائج أن المركبات المعدنية للتكوين , وخصوصًا المسامية ومحتوى الكالسيت, لهما تاثيرا مهما على صلابة التكوين؛ إذ تسفر الفواصل ذات المسامية العالية وقلة محتوى الكالسيت عن أدنى قيم لمقاومة الضغط غير المحصور.

الكلمات الدالة: تقييم الخواص الميكانيكية للصخور، تقييم الصخور مختبريا، قوة الضغط غير المحصورة، حيود الأشعة السينية، المجهر الإلكتروني الماسح.